arXiv:cond-mat/0409168v4 [cond-mat.mes-hall] 12 Sep 2005

Local Spin Anisotropy Effects upon the Magnetization and Specific Heat of Dimer Single Molecule Magnets

Dmitri V. Efremov[1,*] and Richard A. Klemm[2,†]

[1]*Institut für Theoretische Physik, Technische Universität Dresden, 01062 Dresden, Germany*
[2]*Department of Physics, Kansas State University, Manhattan, KS 66506 USA*

(Dated: March 23, 2022)

We present an exactly solvable model of equal spin s_1 dimer single molecule magnets. The spins within each dimer interact via the Heisenberg and the most general quadratic global and local (single-ion) anisotropic spin interactions, and with the magnetic induction $\mathbf{B}$. For antiferromagnetic couplings and $s_1 > 1/2$, the low temperature T magnetization $\boldsymbol{M}(\boldsymbol{B})$ exhibits $2s_1$ steps of universal height and midpoint slope, the sth step of which occurs at the non-universal level-crossing magnetic induction $B^{\rm lc}_{s,s_1}(\theta,\phi)$, where θ,ϕ define the direction of $\boldsymbol{B}$. The specific heat C_V exhibits zeroes as $T \to 0$ at these $B^{\rm lc}_{s,s_1}(\theta,\phi)$ values, which are equally surrounded by universal peak pairs as $T \to 0$. The non-universal $B^{\rm lc}_{s,s_1}(\theta,\phi)$ values lead to a rich variety of magnetization plateau behavior, the structure and anisotropy of which depend upon the various global and local anisotropic spin interaction energies. We solve the model exactly for $s_1 = 1/2$, 1, and 5/2, and present $\boldsymbol{M}(\boldsymbol{B})$ and $C_V(\boldsymbol{B})$ curves at low T for these cases. For weakly anisotropic dimers, rather simple analytic formulas for $\boldsymbol{M}(\boldsymbol{B})$ and $C_V(\boldsymbol{B})$ at arbitrary s_1 accurately fit the exact solutions at sufficiently low T or large B. An expression for $B^{\rm lc}_{s,s_1}(\theta,\phi)$ accurate to second order in the four independent anisotropy energies is derived. Our results are discussed with regard to existing experiments on $s_1 = 5/2$ Fe_2 dimers, suggesting further experiments on single crystals of these and some $s_1 = 9/2$ $[Mn_4]_2$ dimers are warranted.

PACS numbers: 05.20.-y, 75.10.Hk, 75.75.+a, 05.45.-a

INTRODUCTION

Single molecule magnets (SMM's) have been under intense study recently, due to their potential uses in magnetic storage and quantum computing.[1–3] The materials consist of insulating crystalline arrays of identical SMM's 1-3 nm in size, each containing two or more magnetic ions. Since the magnetic ions in each SMM are surrounded by non-magnetic ligands, the intermolecular magnetic interactions are usually negligible. Although the most commonly studied SMM's are the high-spin Mn_{12} and Fe_8,[1–5] such SMM's contain a variety of ferromagnetic (FM) and antiferromagnetic (AFM) intramolecular interactions, rendering unique fits to a variety of experiments difficult.[6]

In addition, there have been many studies of AFM Fe_n ring compounds, where $n = 6, 8, 10, 12$, etc.[7–10] In these studies, analyses of inelastic neutron diffraction data and the magnetic induction $\boldsymbol{B}$ dependence of the low-temperature T specific heat and magnetization steps were made, using the isotropic Heisenberg near-neighbor exchange interaction, the Zeeman interaction, and various near-neighbor spin anisotropy interactions.[7–10] However, the rings were so complicated that analyses of the data using those simple models were inaccessible to present day computers.[8, 9] Thus, those authors used either simulations or phenomenological fits to a first-order perturbation expansion with different spin anisotropy values for each global ring spin value.[8–10]

Here we focus on the simpler cases of equal spin $s_1 = s_2$ magnetic dimers, for which the full spin anisotropy effects can be evaluated analytically, investigated in detail numerically, and compared with experiment. AFM dimers with $s_1 = 1/2, 3/2$,[11–14] and various forms of Fe_2 with $s_1 = 5/2$ were studied recently.[15–20] Several Fe_2 dimers and effective $s_1 = 9/2$ dimers of the type $[Mn_4]_2$,[21, 22] have magnetic interactions weak enough that their effects can be probed at $T \approx 1$K with presently available $\boldsymbol{B}$. A comparison of our results with magnetization $\boldsymbol{M}$ versus $\boldsymbol{B}$ step data on a Fe_2 dimer strongly suggests a substantial presence of local spin anisotropy.[17]

The paper is organized as follows. In Section II, we present the model in the crystal representation and given exact formulas for the matrix elements. The general thermodynamics are presented in Section II, along with the universal behavior of the $M(B)$ and $C_V(B)$ behavior associated with the energy level crossing. In Section IV, we solve the model exactly for $s_1 = 1/2$, giving analytic expressions for the magnetization and specific heat. In Section V, we discuss the exact solution for $s_1 = 1$, present the equations from which the eigenvalues are readily obtained, and give numerical examples of the low-T magnetization and specific heat curves. In Section VI, we present numerical examples of the low-T $s_1 = 5/2$ magnetization and specific heat curves. In section VII, we rotate to the induction representation, and give the eigenstates to first order in the anisotropy energies. These are used to obtain asymptotic expressions for the magnetization and specific heat for arbitrary s_1 that are highly accurate at sufficiently low T and/or large B. In addition, analytic formulas for the magnetic inductions at which the level crossings occur are provided, accurate to sec-

ond order in the anisotropy energies. Finally, in Section VIII we discuss our results with regard to experiments on Fe_2 dimers.

THE MODEL IN THE CRYSTAL REPRESENTATION

We represent the $s_1 = s_2$ dimer quantum states, $|\psi_s^m\rangle$ in terms of the global (total) spin and magnetic quantum numbers s and m, where $\boldsymbol{S} = \boldsymbol{S}_1 + \boldsymbol{S}_2$ and $S_z = \boldsymbol{S}\cdot\hat{\boldsymbol{z}}$ satisfy $\boldsymbol{S}^2|\psi_s^m\rangle = s(s+1)|\psi_s^m\rangle$ and $S_z|\psi_s^m\rangle = m|\psi_s^m\rangle$, where $s = 0, 1, \ldots, 2s_1$, $m = -s, \ldots, s$, and we set $\hbar = 1$. We also have $S_\pm|\psi_s^m\rangle = A_s^{\pm m}|\psi_s^{m\pm1}\rangle$, where $S_\pm = S_x \pm iS_y$ and

$$A_s^m \;=\; \sqrt{(s-m)(s+m+1)}. \tag{1}$$

For an arbitrary $\boldsymbol{B}$, we assume the Hamiltonian has the form $\mathcal{H} = \mathcal{H}_0 + \mathcal{H}_a + \mathcal{H}_b + \mathcal{H}_d + \mathcal{H}_e$, where

$$\mathcal{H}_0 \;=\; -J\boldsymbol{S}^2/2 - \gamma\boldsymbol{S}\cdot\boldsymbol{B} \tag{2}$$

contains the Heisenberg exchange and Zeeman interactions, the gyromagnetic ratio $\gamma = g\mu_B$, where $g \approx 2$ and μ_B is the Bohr magneton. The global axial and azimuthal anisotropy terms

$$\mathcal{H}_b \;=\; -J_bS_z^2 \tag{3}$$

and

$$\mathcal{H}_d \;=\; -J_d(S_x^2 - S_y^2), \tag{4}$$

respectively, only involve components of $\boldsymbol{S}$, but have been the main anisotropy terms discussed in the SMM literature,[5, 21] so we have included them for comparison. Such terms have been commonly studied as an effective Hamiltonian for a singlet orbital ground state, in which the tensor global spin interaction with a fixed spin quantum number s has the form $\boldsymbol{S}\cdot\overleftrightarrow{\boldsymbol{\Lambda}}\cdot\boldsymbol{S}$, resulting in the principal axes x, y and z.[23] For a dimer, we take $\overleftrightarrow{\boldsymbol{\Lambda}}$ to be diagonal in the orientation pictured in Fig. 1. Then $J = -(\Lambda_{xx} + \Lambda_{yy})/2$, $J_b = -\Lambda_{zz} + (\Lambda_{xx} + \Lambda_{yy})/2$, and $J_d = (\Lambda_{yy} - \Lambda_{xx})/2$. Taking $|J_d/J| \ll 1$ and $|J_b/J| \ll 1$ still leaves J_d/J_b unrestricted. The single-ion axial and azimuthal anisotropy terms,

$$\mathcal{H}_a \;=\; -J_a\sum_{i=1}^{2} S_{iz}^2 \tag{5}$$

and

$$\mathcal{H}_e \;=\; -J_e\sum_{i=1}^{2}\Big(S_{ix}^2 - S_{iy}^2\Big), \tag{6}$$

respectively, arise from spin-orbit interactions of the local crystal field with the individual spins. These terms have usually been neglected in the SMM literature, but have been studied with regard to complexes containing a single magnetic ion, such as Ni^{+2},[23] and with regard to clusters of larger numbers of identical magnetic ions.[23, 24]

The local axially and azimuthally anisotropic exchange interactions

$$\mathcal{H}_f \;=\; -J_fS_{1z}S_{2z}, \tag{7}$$

$$\mathcal{H}_c \;=\; -J_c(S_{1x}S_{2x} - S_{1y}S_{2y}), \tag{8}$$

satisfy

$$2\mathcal{H}_f/J_f \;=\; \mathcal{H}_b/J_b - \mathcal{H}_a/J_a, \tag{9}$$

$$2\mathcal{H}_c/J_c \;=\; \mathcal{H}_d/J_d - \mathcal{H}_e/J_e, \tag{10}$$

so we need only include either either $\mathcal{H}_a$ or $\mathcal{H}_f$ and $\mathcal{H}_e$ or $\mathcal{H}_c$, respectively.[23] That is, if we stick to the Hamiltonian $\mathcal{H}$, we may incorporate the effects of $\mathcal{H}_f$ and $\mathcal{H}_c$ by letting $J_b \to J_b + J_f/2$, $J_a \to J_a - J_f/2$, and $J_d \to J_d + J_c/2$, $J_e \to J_e - J_c/2$, respectively. Since $\mathcal{H}_a$ and $\mathcal{H}_e$ describe the axial and azimuthal anisotropy each single ion attains from its surrounding environment, they are the physically relevant local anisotropy interactions.

For the case of Fe_2,[15] a constituent of the high-spin SMM Fe_8 and the AFM Fe_n rings,[4, 8, 9] the exchange between the Fe^{+3} $s_1 = 5/2$ spins occurs via two oxygen ions, and these four ions essentially lie in the same (xz) plane.[15, 18] We set the z axis parallel to the dimer axis, as pictured in Fig. 1. Since the quantization axis is along the dimer axis, which is fixed in a crystal, we denote this representation as the crystal representation.

We generally expect each of the J_j for $j = a, b, d, e$ to satisfy $|J_i/J| \ll 1$, but there are not generally any other restrictions upon the various magnitudes of the J_j. Since all dimers known to date have predominantly AFM couplings ($J < 0$), and also because their magnetizations and specific heats are particularly interesting, we shall only consider AFM dimers. In addition, since no studies on unequal-spin dimers have been reported to our knowledge, we shall only treat the equal-spin $s_1 = s_2$ case. We note that for equal spin dimers, the group symmetry of the dimer environment is C_{2v}, so that Dzaloshinskiĭ-Moriya interactions do not arise.[23] Hence, our Hamiltonian $\mathcal{H}$ is the most general quadratic anisotropic spin Hamiltonian of an equal-spin dimer.

For $\boldsymbol{B} = B(\sin\theta\cos\phi, \sin\theta\sin\phi, \cos\theta)$, we have

$$\mathcal{H}_0|\psi_s^m\rangle \;=\; E_s^m|\psi_s^m\rangle + \delta E\sum_{\sigma=\pm1} e^{-i\sigma\phi}A_s^{\sigma m}|\psi_s^{m+\sigma}\rangle, \tag{11}$$

$$\mathcal{H}_b|\psi_s^m\rangle \;=\; -J_bm^2|\psi_s^m\rangle, \tag{12}$$

and

$$\mathcal{H}_d|\psi_s^m\rangle \;=\; \frac{-J_d}{2}\sum_{\sigma=\pm1} F_s^{\sigma m}|\psi_s^{m+2\sigma}\rangle, \tag{13}$$

where

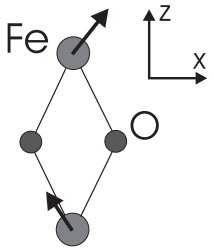


FIG. 1: Sketch of an Fe_2 dimer, with two bridging O^{-2} ions (O). Ligands (not pictured) are attached to the Fe^{+3} ions (Fe). The arrows signify spins.

$$E_s^m = -Js(s+1)/2 - mb\cos\theta, \quad (14)$$

$$\delta E = -\frac{1}{2}b\sin\theta, \quad (15)$$

$$b = \gamma B. \quad (16)$$

and

$$F_s^x = A_s^x A_s^{1+x}. \quad (17)$$

$\mathcal{H}_a$ and $\mathcal{H}_c$ contain the individual spin operators S_{iz} and $S_{i\pm}$ for $i = 1, 2$. After some Clebsch-Gordon algebra involving the Wigner-Eckart theorem, for arbitrary (s_1, s, m),

$$S_{i\pm}|\psi_s^m\rangle = \frac{1}{2}A_s^{\pm m}|\psi_s^{m\pm1}\rangle \mp \frac{1}{2}(-1)^i\Big(C_{s,s_1}^{\pm m}|\psi_{s-1}^{m\pm1}\rangle - C_{s+1,s_1}^{-1\mp m}|\psi_{s+1}^{m\pm1}\rangle\Big), \quad (18)$$

$$S_{iz}|\psi_s^m\rangle = \frac{m}{2}|\psi_s^m\rangle - \frac{1}{2}(-1)^i\Big(D_{s,s_1}^m|\psi_{s-1}^m\rangle + D_{s+1,s_1}^m|\psi_{s+1}^m\rangle\Big), \quad (19)$$

where

$$C_{s,s_1}^m = \sqrt{(s-m)(s-m-1)}\eta_{s,s_1}, \quad (20)$$

$$D_{s,s_1}^m = \sqrt{(s^2-m^2)}\eta_{s,s_1}, \quad (21)$$

and

$$\eta_{s,s_1} = \sqrt{[(2s_1+1)^2 - s^2]/(4s^2-1)}. \quad (22)$$

For $s = 0$, we require $m = 0$, for which $C_{0,s_1}^0 = D_{0,s_1}^0 = 0$. We then find

$$\mathcal{H}_a|\psi_s^m\rangle = \frac{-J_a}{2}\Big(G_{s,s_1}^m|\psi_s^m\rangle + \sum_{\sigma'=\pm1} H_{s,s_1}^{m,\sigma'}|\psi_{s+2\sigma'}^m\rangle\Big), \quad (23)$$

$$\mathcal{H}_e|\psi_s^m\rangle = -\frac{J_e}{4}\sum_{\sigma=\pm1}\Big(L_{s,s_1}^{\sigma m}|\psi_s^{m+2\sigma}\rangle + \sum_{\sigma'=\pm1} K_{s,s_1}^{\sigma m,\sigma'}|\psi_{s+2\sigma'}^{m+2\sigma}\rangle\Big), \quad (24)$$

$$G_{s,s_1}^m = s(s+1) - 1 + [m^2 + 1 - 2s(s+1)]\alpha_{s,s_1}, \quad (25)$$

$$H_{s,s_1}^{m,\sigma'} = D_{s+(\sigma'+1)/2,s_1}^m D_{s+(3\sigma'+1)/2,s_1}^m, \quad (26)$$

$$K_{s,s_1}^{x,\sigma'} = C_{s+(\sigma'+1)/2,s_1}^{-\sigma' x-(1+\sigma')/2} C_{s+(3\sigma'+1)/2,s_1}^{-\sigma' x-(3\sigma'+1)/2}, \quad (27)$$

$$L_{s,s_1}^x = 2F_s^x\alpha_{s,s_1}, \quad (28)$$

and

$$\alpha_{s,s_1} = \frac{3s(s+1) - 4s_1(s_1+1) - 3}{(2s-1)(2s+3)}. \quad (29)$$

We note that $\alpha_{s,s_1} = 1 - \eta_{s,s_1}^2 - \eta_{s+1,s_1}^2$ and that Eq. (29) holds for $s \geq 0$. Equations (18) and (19) allow for an exact solution to the most general Hamiltonian of arbitrary order in the individual spin operators. In all previous treatments of more complicated spin systems with similar anisotropic interactions, it was only possible to obtain numerical solutions, and therefore the full anisotropy of the magnetization and specific heat was not calculated.[23, 24] The operations of $\mathcal{H}_0$, $\mathcal{H}_b$ and $\mathcal{H}_d$ satisfy the selection rules $\Delta s = 0$, $\Delta m = 0, \pm1, \pm2$. The local anisotropy interactions $\mathcal{H}_a$ and $\mathcal{H}_e$ allow transitions satisfying $\Delta s = 0, \pm2$, $\Delta m = 0$, and $\Delta s = 0, \pm2$, $\Delta m = \pm2$, respectively, so in the presence of either of these interactions, s is no longer a good quantum number, unless $s_1 = 1/2$.

GENERAL THERMODYNAMICS

In order to obtain the thermodynamic properties, we first calculate the canonical partition function, $Z = \mathrm{Tr}\exp(-\beta\mathcal{H})$. Since $\mathcal{H}$ is not diagonal in the (s, m) representation, we must construct the wave function from all possible spin states. We then write

$$Z = \mathrm{Tr}\langle\Psi_{s_1}|e^{-\beta\mathcal{H}}|\Psi_{s_1}\rangle, \quad (30)$$

where $|\Psi_{s_1}$ is constructed from the $\{|\psi_s^m\rangle\}$ basis as

$$\langle\Psi_{s_1}| = \Big(< \psi_{2s_1}^{2s_1}|, \langle\psi_{2s_1}^{2s_1-1}|, \ldots, \langle\psi_1^0|, \langle\psi_1^{-1}|, \langle\psi_0^0|\Big), \quad (31)$$

where $\beta = 1/(k_BT)$ and k_B is Boltzmann's constant. To evaluate the trace, it is useful to diagonalize the $\langle\Psi_{s_1}|\mathcal{H}|\Psi_{s_1}\rangle$ matrix. To do so, we let $|\Psi_{s_1}\rangle = \boldsymbol{U}|\Phi_{s_1}\rangle$, where

$$\langle\Phi_{s_1}| = \Big(\langle\phi_{n_{s_1}}|, \langle\phi_{n_{s_1}-1}|, \ldots, \langle\phi_1|\Big), \quad (32)$$

is constructed from the new orthonormal basis $\{|\phi_n\rangle\}$, and $\boldsymbol{U}$ is a unitary matrix of rank $n_{s_1} = (2s_1 + 1)^2$. Choosing $\boldsymbol{U}$ to diagonalize $\mathcal{H}$, we generally obtain $\mathcal{H}|\phi_n\rangle = \epsilon_n|\phi_n\rangle$ and the partition function for a SMM dimer,

$$Z = \sum_{n=1}^{n_{s_1}}\exp(-\beta\epsilon_n). \quad (33)$$

The specific heat $C_V = k_B\beta^2\partial^2 \ln Z/\partial\beta^2$ is then easily found at all $T, \boldsymbol{B}$,

$$C_V = \frac{k_B\beta^2}{Z^2}\Big[Z\sum_{n=1}^{n_{s_1}}\epsilon_n^2 e^{-\beta\epsilon_n} - \Big(\sum_{n=1}^{n_{s_1}}\epsilon_n e^{-\beta\epsilon_n}\Big)^2\Big]. \quad (34)$$

It is easily seen from Eq. (34) that at the induction $B^{\rm lc}_{s,s_1}$ corresponding to the sth level crossing in which $\epsilon_s = \epsilon_{s-1}$, $C_V \to 0$ as $T \to 0$. The magnetization

$$\boldsymbol{M} = \frac{1}{Z}\sum_{n=1}^{n_{s_1}} \boldsymbol{\nabla}_{\boldsymbol{B}}(\epsilon_n)\exp(-\beta\epsilon_n), \quad (35)$$

requires $\boldsymbol{\nabla}_{\boldsymbol{B}}(\epsilon_n)$ for each $\boldsymbol{B}$. As $T \to 0$, at most two eigenstates are relevant. For most B values, only one ϵ_n is important. But near the sth level-crossing induction $B^{\rm lc}_{s,s_1}(\theta,\phi)$ at which $\epsilon_s = \epsilon_{s-1}$, two eigenstates are relevant. We then have

$$C_V\Big[B^{\rm lc}_{s,s_1}(\theta,\phi)\Big] \underset{T\to 0}{\to} 0, \quad (36)$$

$$C_V\Big[B^{\rm lc}_{s,s_1}(\theta,\phi) \pm \frac{2c}{\gamma\beta}\Big] \underset{k_BT\ll|J|}{\to} C_V^{\rm peak} \quad (37)$$

$$C_V^{\rm peak}/k_B = \Big(\frac{c}{\cosh c}\Big)^2 \approx 0.439229, \quad (38)$$

and

$$M\Big[B^{\rm lc}_{s,s_1}(\theta,\phi)\Big]/\gamma \underset{T\to 0}{\to} s - \frac{1}{2}, \quad (39)$$

$$\frac{dM}{\gamma dB}\Big|_{B^{\rm lc}_{s,s_1}(\theta,\phi)} = \frac{\beta\gamma}{4}, \quad (40)$$

where $s = 1, \ldots, 2s_1$ and $c \approx 1.19967864$ is the solution to $\tanh c = 1/c$. The easiest way to obtain Eq. (39) is to first rotate the crystal so the quantization axis is along $\boldsymbol{B}$, as discussed in Appendix B. We note that $B^{\rm lc}_{s,s_1}(\theta,\phi)$ depends upon s, s_1, and the direction of $\boldsymbol{B}$ when anisotropic interactions are present. Hence, the heights and midpoint slopes of the $2s_1$ $M(B)$ steps are universal, but the step positions and hence their plateaus are not. Correspondingly, the $2s_1$ positions of the $C_V(B)$ zeroes are non-universally spaced, but each zero is equally surrounded by two peaks of equal, universal height, the universal spacing between which is $\propto T$ as $T \to 0$. Hence, the non-universal level-crossing inductions $B^{\rm lc}_{s,s_1}(\theta,\phi)$ fully determine the low-T thermodynamics of AFM dimers. In the next three sections, we consider the special cases of $s_1 = 1/2, 1$ and $5/2$. Then, in Section VII and Appendix D, we present out general expression for $B^{\rm lc}_{s,s_1}(\theta,\phi)$ accurate to second order in each of the J_j. We remark that a double peak in the low-T $C_V(B)$ curve has been seen experimentally in a much more complicated Fe_6 ring compound, and was attributed to level crossing.[8]

ANALYTIC RESULTS FOR SPIN 1/2

Plots of C_V/k_B and M/γ versus $\gamma B/|J|$ for the isotropic spin 1/2 dimer were given previously.[14] For $s_1 = 1/2$ with an arbitrary $\boldsymbol{B}$ and J_j for $j = a, b, d, e$, the rank 4 Hamiltonian matrix is block diagonal, since $s = 0, 1$ is a good quantum number. The eigenvalues are given by

$$\epsilon_1 = -\frac{J_a}{2}, \quad (41)$$

$$\epsilon_n = -\frac{J_a}{2} - J + \lambda_n, \qquad n = 2, 3, 4, \quad (42)$$

where

$$0 = \lambda_n^3 + 2\lambda_n^2 J_b - \lambda_n[J_d^2 - J_b^2 + b^2] - b^2\sin^2\theta[J_b - J_d\cos(2\phi)]. \quad (43)$$

For the special cases $\boldsymbol{B}||\hat{\boldsymbol{i}}$ for $i = x, y, z$, the λ_n^i satisfy

$$\lambda_n^z = 0, -J_b \pm F_z, \quad (44)$$

$$\lambda_n^{x,y} = -2J_{y,x},\ -J_{x,y} \pm F_{x,y}, \quad (45)$$

where

$$F_i = \sqrt{b^2 + J_i^2}, \quad (46)$$

$$J_{x,y,z} = (J_b \pm J_d)/2,\ J_d, \quad (47)$$

respectively, and where J_x (J_y) corresponds to the upper (lower) sign.

The magnetization for $\boldsymbol{B}||\hat{\boldsymbol{i}}$ is given by

$$M_i = \frac{\gamma^2 B\sinh(\beta F_i)}{F_i\mathcal{D}_i}, \quad (48)$$

$$\mathcal{D}_i = \cosh(\beta F_i) + \Delta_i/2, \quad (49)$$

$$\Delta_{x,y} = \exp(-\beta J_{x,y})[\exp(-\beta J) + \exp(2\beta J_{x,y})], \quad (50)$$

$$\Delta_z = \exp(-\beta J_b)[\exp(-\beta J) + 1], \quad (51)$$

respectively. When the interactions are written in terms of the less physical J_f, J_b, J_d, and J_c, then $J_b \to J_b + J_f$ and $J_d \to J_d + J_c/2$, so that for $s_1 = 1/2$, J_f and J_c merely renormalize J_b and J_d. Neither of the single-ion spin anisotropy terms $\mathcal{H}_a$ and $\mathcal{H}_e$ affect the thermodynamics for $s_1 = 1/2$. We note that $M_y(J_d) = M_x(-J_d)$ for each B, as expected from $\mathcal{H}_d = -J_d(S_x^2 - S_y^2)$.

From Eqs. (41), (42), (44), and (45), the single level crossing induction ($s = 1$) for am $s_1 = 1/2$ dimer with $\boldsymbol{B}||\hat{\boldsymbol{i}}$ occurs at

$$\gamma B^{\rm lc}_{1,1/2} = \begin{cases} \sqrt{J^2 + J(J_b \pm J_d)}, & \boldsymbol{B}||\hat{\boldsymbol{x}}, \hat{\boldsymbol{y}} \\ \sqrt{(J + J_b)^2 - J_d^2}, & \boldsymbol{B}||\hat{\boldsymbol{z}} \end{cases}, \quad (52)$$

provided that $J + J_{x,y} < 0$ and $J + J_b < 0$, respectively.

To distinguish the different effects of the global anisotropy interactions J_b and J_d that affect the magnetization of $s_1 = 1/2$ dimers, in Figs. 2 and 3, we

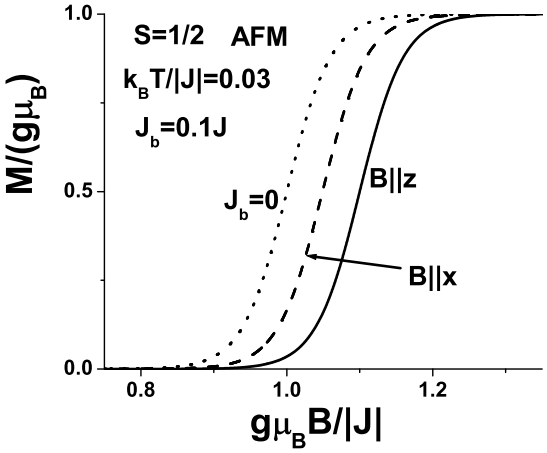


FIG. 2: Plots of M/γ versus $\gamma B/|J|$ at $k_BT/|J| = 0.03$ for the AFM spin 1/2 dimer with $J_b = 0.1J$, $J_d = 0$, with $\boldsymbol{B}||\hat{\boldsymbol{z}}$ (solid), $\boldsymbol{B}||\hat{\boldsymbol{x}}$ (dashed), along with the isotropic case $J_b = J_d = 0$ (dotted).

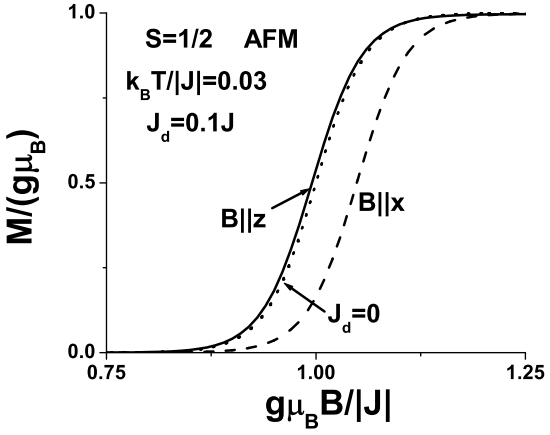


FIG. 3: Plots of M/γ versus $\gamma B/|J|$ at $k_BT/|J| = 0.03$ for the AFM spin 1/2 dimer with $J_d = 0.1J$, $J_b = 0$, with $\boldsymbol{B}||\hat{\boldsymbol{z}}$ (solid), $\boldsymbol{B}||\hat{\boldsymbol{x}}$ (dashed), along with the isotropic case $J_b = J_d = 0$ (dotted).

have respectively plotted the low-T M/γ versus $\gamma B/|J|$ with $J_b = 0.1J, J_d = 0$ and $J_d = 0.1J, J_b = 0$ for $\boldsymbol{B}|||\hat{\boldsymbol{z}}$ (solid) and $\boldsymbol{B}||\hat{\boldsymbol{x}}$ (dashed), along with the isotropic case $J_b = J_d = 0$ (dotted). From Fig. 2, $J_b < 0$ and $J_d = 0$ causes a greater shift to higher B values at the magnetization step with $\boldsymbol{B}||\hat{\boldsymbol{z}}$ than for $\boldsymbol{B}||\hat{\boldsymbol{x}}$, consistent with Eq. (52). In addition, J_d finite with $J_b = 0$ has a very different effect upon the anisotropy of the magnetization step, as shown in Fig. 3. Although for $\boldsymbol{B}||\hat{\boldsymbol{z}}$, B at the step is slightly reduced from its isotropic interaction value, for $\boldsymbol{B}||\hat{\boldsymbol{x}}$, the magnetization step occurs at a larger B. These results are consistent with Eq. (52). The midpoint slopes are universal, in accordance with Eq. (**??**slope).

The specific heat of an $s_1 = 1/2$ dimer with $\boldsymbol{B}||\hat{\boldsymbol{i}}$ is

$$C_{Vi} \;=\; \frac{k_B\beta^2\mathcal{N}_i}{\mathcal{D}_i^2}, \tag{53}$$

where the $\mathcal{D}_i$ are given by Eq. (49), and the $\mathcal{N}_i$ are given in Appendix A. Plots at low T of C_V/k_B versus $\gamma B/|J|$ for $s_1 = 1/2$ dimers with the corresponding global anisotropies $J_b = 0.1J$ and $J_d = 0.1J$ are shown in Figs. 4 and 5, respectively. We note the universal curve shapes, but non-universal level-crossing positions, in quantitative agreement with Eqs. (36)-(38). In Fig. 4, the positions of the maxima and the central minimum in C_V track that of the magnetization step in Fig. 2 with the same parameters. With $J_d = 0.1J$, the behaviors in C_V and M for $\boldsymbol{B}||\hat{\boldsymbol{x}}$ are also very similar. However, there is a slight difference in the behaviors for $\boldsymbol{B}||\hat{\boldsymbol{z}}$. Note that M (Fig. 3) shows a slight reduction for $\boldsymbol{B}||\hat{\boldsymbol{z}}$ in the induction required for the step, whereas C_V (Fig. 5) shows a slight increase in the positions of the peaks. This detail only appears when $J_d \neq 0$, for which the effective temperature

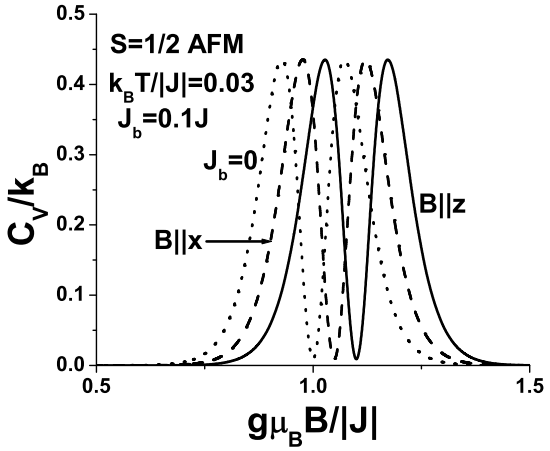


FIG. 4: Plot of C_V/k_B versus $\gamma B/|J|$ for the AFM spin 1/2 dimer with $J_b = 0.1J, J_d = 0$ at $k_BT/|J| = 0.03$ with the same curve notation as in Fig. 2.

is slightly higher than for $J_d = 0$.

ANALYTIC AND NUMERICAL RESULTS FOR SPIN 1

For dimers with $s_1 = 1$, the allowed s values are $s = 0, 1, 2$. The three $s = 1$ states are decoupled from the six remaining $s = 0, 2$ states. They satisfy a cubic equation given in Appendix A. For $\boldsymbol{B}||\hat{\boldsymbol{i}}$ with $i = x, y, z$, this cubic equation simplifies to a linear and a quadratic equation, as for the $s = 1$ eigenstates of $s_1 = 1/2$ dimers.

The remaining six eigenstates corresponding nominally

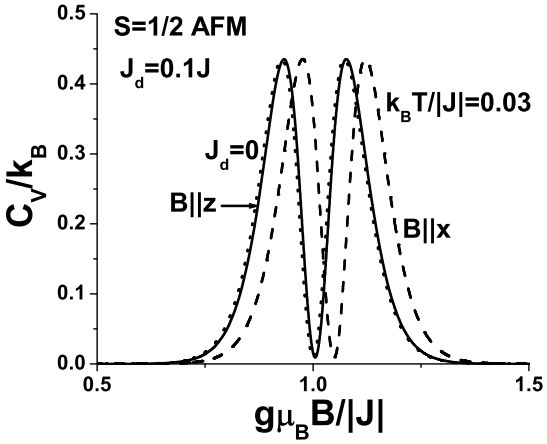


FIG. 5: Plot of C_V/k_B versus $\gamma B/|J|$ for the AFM spin 1/2 dimer with $J_d = 0.1J$, $J_b = 0$ at $k_BT/|J| = 0.03$ with the same curve notation as in Fig. 3.

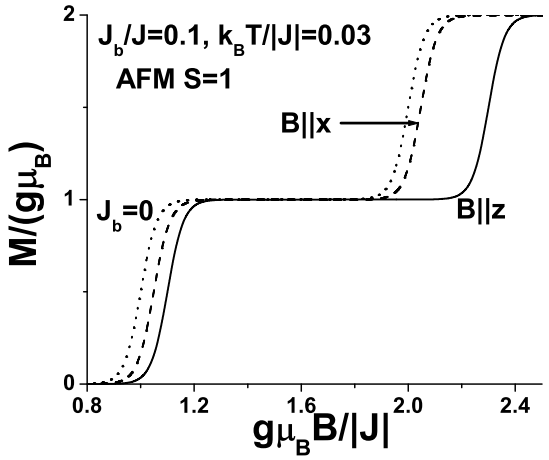


FIG. 6: Plot at $k_BT/|J| = 0.03$ and $J_b/J = 0.1$ of M/γ versus $\gamma B/|J|$ for the AFM spin 1 dimer. Curves for $\boldsymbol{B}||\hat{\boldsymbol{z}}$ (solid), $\boldsymbol{B}||\hat{\boldsymbol{x}}$ (dashed), and the isotropic case ($J_b = 0$, dotted) are shown.

to $s = 0, 2$ are in general all mixed. The matrix leading to the hexatic equation from which the six eigenvalues can be obtained is given in Appendix A. That is sufficient to evaluate the eigenvalues for $s_1 = 1$ using symbolic manipulation software. When combined with the three $s = 1$ eigenvalues, one can then use Eqs. (34) and (35) to obtain the resulting exact magnetization and specific heat at an arbitrary $\boldsymbol{B}$. The combined nine eigenvalues depend upon all four anisotropy parameters J_j for $j = a, b, d, e$.

To the extent that the eigenvalues can be obtained from the solutions to either linear or quadratic equations, the expressions for the $B^{\rm lc}_{s,1}$ are simple, and are given in Appendix A. In the global anisotropy case $J_a = J_e = 0$, the first level crossing induction $B^{\rm lc}_{1,1}$ with $\boldsymbol{B}||\hat{\boldsymbol{i}}$ is identical to $B^{\rm lc}_{1,1/2}$, the level crossing with $s_1 = 1/2$ given by Eq. (52). For comparison, we expand the first and second level crossing inductions to first order in each of the J_j for $j = a, b, d, e$ for $\boldsymbol{B}||\hat{\boldsymbol{i}}$ where $i = x, y, z$,

$$\gamma B^{\rm lc(1)}_{1,1,z} = -J + \frac{J_a}{3} - J_b, \quad (54)$$

$$\gamma B^{\rm lc(1)}_{1,1,x,y} = -J - \frac{J_a}{6} - \frac{J_b}{2} \mp \frac{1}{2}(J_d - J_e), \quad (55)$$

$$\gamma B^{\rm lc(1)}_{2,1,z} = -2J - J_a - 3J_b, \quad (56)$$

$$\gamma B^{\rm lc(1)}_{2,1,x,y} = -2J + \frac{J_a}{2} - \frac{J_b}{2} \mp \frac{5J_d}{2} \mp \frac{3J_e}{2}, \quad (57)$$

where the upper (lower) sign is for $\boldsymbol{B}||\hat{\boldsymbol{x}}$ ($\boldsymbol{B}||\hat{\boldsymbol{y}}$), respectively.

From these simple first-order results, it is possible to understand the qualitatively different behavior obtained with local, single-ion, anisotropy from that obtained with global anisotropy. In the isotropic case $J_j = 0 \forall j$, the first and second level crossings occur at $-J$ and $-2J$, respectively. For each induction direction, the signs of the J_b and J_d contributions to $B^{\rm lc(1)}_{2,1} + 2J$ and $B^{\rm lc(1)}_{1,1} + J$ are the same, whereas the signs of the J_a and J_e contributions to $B^{\rm lc(1)}_{2,1} + 2J$ and $B^{\rm lc(1)}_{1,1} + J$ are the *opposite*.

In Figs. 6-15, we plot M/γ and C_V/k_B versus $\gamma B/|J|$ for five low-T cases of AFM $s_1 = 1$ dimers, taking $k_BT/|J| = 0.03$. The M/γ curves all exhibit the universal features predicted by Eqs. (39) and (40). The corresponding C_V/k_B curves also obey the universal features predicted in Eqs. (36)-(38). In these figures, only one of the five anisotropy interactions J_j is non-vanishing, and we take $J_j/J = 0.1$, for $j = b, d, a, e$, and c, respectively. Unlike the case of $s_1 = 1/2$ dimers, for which J_c merely renormalizes J_d, for $s_1 = 1$ all of these interactions lead to distinct anisotropy effects in the low-T magnetization and specific heat. Of course, since the case $J_c = 0.1J$ (and the remaining $J_j = 0$) can be evaluated by setting $J_d = 0.05J$ and $J_e = -0.05J$ for any s_1, it is not really distinct from the other anisotropy interactions, but only represents that particular combination of global and local azimuthal anisotropy interactions.

We first show the results for the global anisotropy interactions. In Figs. 6 and 7, we plot $M(B)$ and $C_V(B)$ for $J_b = 0.1J$ (and all other $J_j = 0$) at $k_BT/|J| = 0.03$ for the AFM $s_1 = 1$ dimer. The level-crossing induction increases monotonically with level-crossing number, with the largest induction required occurring for $\boldsymbol{B}||\hat{\boldsymbol{z}}$, as for $s_1 = 1/2$, quantitatively consistent with Eqs. (54)-(57). In Figs. 8 and 9, the corresponding results for $J_d = 0.1J$ (and the other $J_j = 0$) are shown. Again, the level-crossing induction increases monotonically with level-crossing number, and the largest induction required

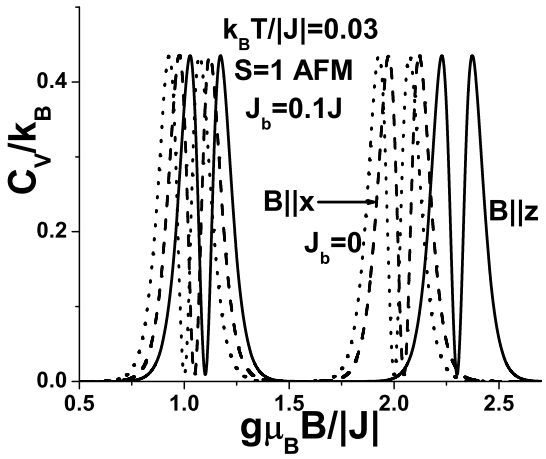


FIG. 7: Plot at $k_BT/|J| = 0.03$ and $J_b/J = 0.1$ of C_V/k_B versus $\gamma B/|J|$ for the AFM spin 1 dimer. Curves for $\boldsymbol{B}||\hat{\boldsymbol{z}}$ (solid), $\boldsymbol{B}||\hat{\boldsymbol{x}}$ (dashed), and the isotropic case ($J_b = 0$, dotted) are shown.

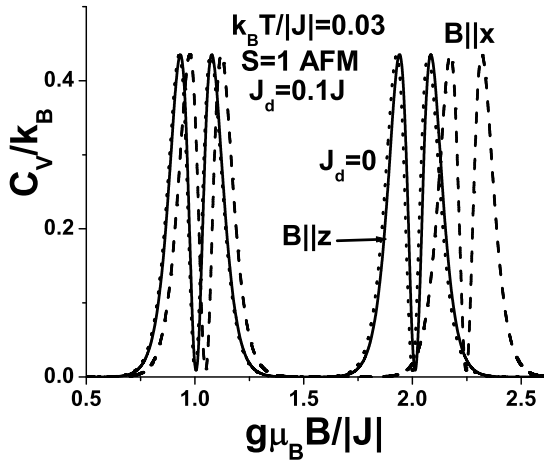


FIG. 9: Plot at $k_BT/|J| = 0.03$ and $J_d/J = 0.1$ of C_V/k_B versus $\gamma B/|J|$ for the AFM spin 1 dimer. Curves for $\boldsymbol{B}||\hat{\boldsymbol{z}}$ (solid), $\boldsymbol{B}||\hat{\boldsymbol{x}}$ (dashed), and the isotropic case ($J_b = 0$, dotted) are shown.

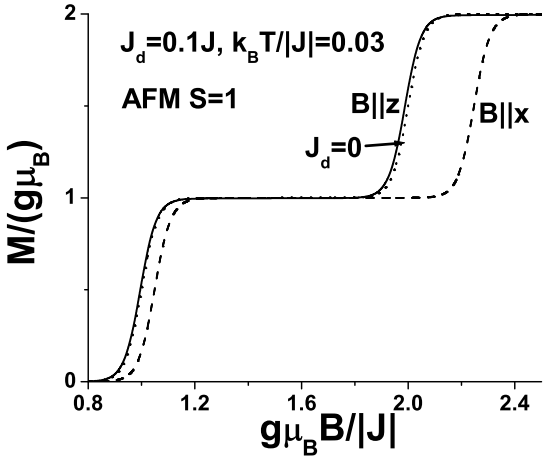


FIG. 8: Plot at $k_BT/|J| = 0.03$ and $J_d/J = 0.1$ of $\boldsymbol{M}/\gamma$ versus $\gamma B/|J|$ for the AFM spin 1 dimer. Curves for $\boldsymbol{B}||\hat{\boldsymbol{z}}$ (solid), $\boldsymbol{B}||\hat{\boldsymbol{x}}$ (dashed), and the isotropic case ($J_d = 0$, dotted) are shown.

for each level crossing occurs for $\boldsymbol{B}||\hat{\boldsymbol{x}}$, quantitatively consistent with Eqs. (54)-(57), as for $s_1 = 1/2$. We note that the solid curves for $\boldsymbol{B}||\hat{\boldsymbol{z}}$ are nearly identical with the dotted curves for the isotropic case $J_j = 0 \forall j$. However, there is a very small distinction between these M and C_V curves. This distinction is also present for $s_1 = 1/2$, as shown in Figs. 3 and 5, and is a detail of the shapes of the M and C_V curves arising from a slightly higher effective temperature with $J_d \neq 0$ than in the other cases studied.

Next, in Figs. 10-13, we show the corresponding curves for $M(B)$ and $C_V(B)$ at low T for the local anisotropies $J_a = 0.1J$ and $J_e = 0.1J$, respectively, with the other $J_j = 0$. In contrast to the global anisotropies, the increase in B required with the level crossing is not monotonic in the level-crossing number, quantitatively consistent with Eqs. (54)-(57). In particular, we note that in each of these figures, the deviations in the level crossings $B^{\rm lc}_{2,1} + 2J$ and $B^{\rm lc}_{1,1} + J$ are opposite in sign.

A careful examination of the exact formula for C_V reveals that it vanishes at precisely the level crossing inductions as $T \to 0$. Similarly, the magnetization curve attains its midpoint values $\frac{1}{2}$ and $\frac{3}{2}$ between the two neighboring steps at the level crossing inductions as $T \to 0$.

Finally, in Figs. 14 and 15, we show the corresponding $M(B)$ and $C_V(B)$ curves for $J_c = 0.1J$, corresponding to the parameter choices $J_e = -0.05J$ and $J_d = 0.05J$. With this combination, the magnetization and specific heat curves shown in Figs. 14 and 15 resemble those for $J_d = 0.1J$ shown in Figs. 8 and 9, except that the second magnetization steps and the second set of specific heat peaks have nearly the same behavior as do the first magnetization steps and specific heat double peaks.

In short, the case $s_1 = 1$, for which the exact expressions from which the eigenvalues can be readily obtained are sufficiently short as to be writable on paper, are sufficient to exhibit the very different behaviors obtained from the single-ion, local spin anisotropy interactions from those obtained from the global spin anisotropy interactions. As s_1 increases beyond 1, the situation becomes not only more complicated, but also more interesting, as shown in the following.

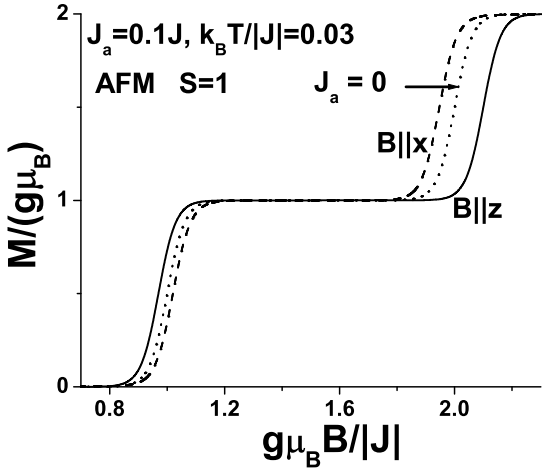


FIG. 10: Plot at $k_BT/|J| = 0.03$ and $J_a/J = 0.1$ of M/γ versus $\gamma B/|J|$ for the AFM spin 1 dimer. Curves for $\boldsymbol{B}||\hat{\boldsymbol{z}}$ (solid), $\boldsymbol{B}||\hat{\boldsymbol{x}}$ (dashed), and the isotropic case ($J_a = 0$, dotted) are shown.

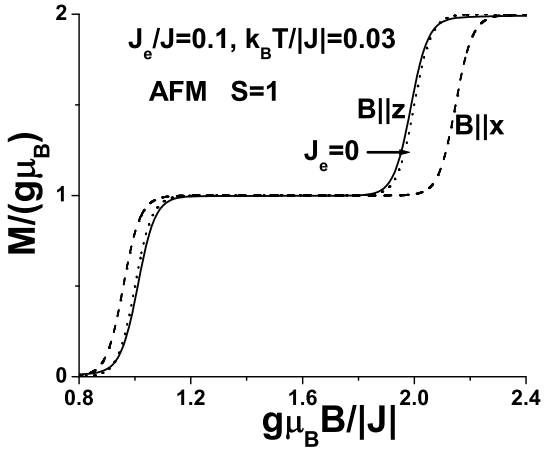


FIG. 12: Plot at $k_BT/|J| = 0.03$ and $J_e/J = 0.1$ of M/γ versus $\gamma B/|J|$ for the AFM spin 1 dimer. Curves for $\boldsymbol{B}||\hat{\boldsymbol{z}}$ (solid), $\boldsymbol{B}||\hat{\boldsymbol{x}}$ (dashed), and the isotropic case ($J_e = 0$, dotted) are shown.

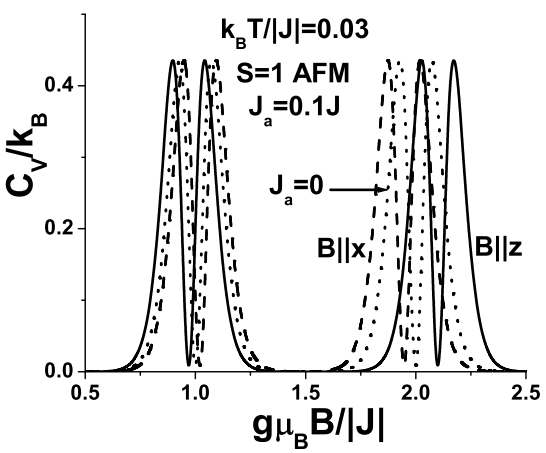


FIG. 11: Plot at $k_BT/|J| = 0.03$ and $J_a/J = 0.1$ of C_V/k_B versus $\gamma B/|J|$ for the AFM spin 1 dimer. Curves for $\boldsymbol{B}||\hat{\boldsymbol{z}}$ (solid), $\boldsymbol{B}||\hat{\boldsymbol{x}}$ (dashed), and the isotropic case ($J_b = 0$, dotted) are shown.

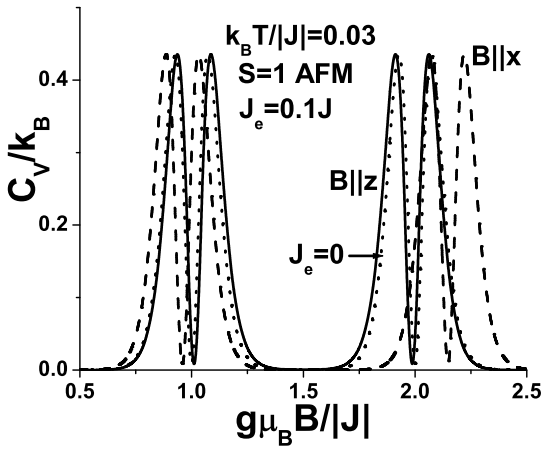


FIG. 13: Plot at $k_BT/|J| = 0.03$ and $J_b/J = 0.1$ of C_V/k_B versus $\gamma B/|J|$ for the AFM spin 1 dimer. Curves for $\boldsymbol{B}||\hat{\boldsymbol{z}}$ (solid), $\boldsymbol{B}||\hat{\boldsymbol{x}}$ (dashed), and the isotropic case ($J_b = 0$, dotted) are shown.

EXACT NUMERICAL RESULTS FOR SPIN 5/2

For $s_1 = 5/2$, one of the cases of greatest experimental interest, when $\mathcal{H}_a$ and $\mathcal{H}_e$ are present, none of the allowed s, m values is a true quantum number. That is, $\mathcal{H}_a$ and $\mathcal{H}_e$ cause all of the states with nominally odd or even s to mix with one another. For $\boldsymbol{B}||\hat{\boldsymbol{i}}$ for $i = x, y, z$, this simplifies in the crystal representation as for $s_1 = 1$, since only states with odd or even m in the appropriately chosen representation can mix. By using symbolic manipulation software, it is possible to solve for the exact eigenvalues of the $s_1 = 5/2$ dimer. However, because the analytic expressions for the eigenvalues are much more complicated than those for $s_1 = 1$ presented in Appendix A, we shall not attempt to present them, but will instead focus upon their numerical evaluation for specific cases.

To first order in the J_j, the first three level crossings for $\boldsymbol{B}||\hat{\boldsymbol{i}}$ with $i = x, y, z$ are

$$\gamma B^{\mathrm{lc}(1)}_{1,5/2,z} = -J + \frac{32J_a}{15} - J_b, \tag{58}$$

$$\gamma B^{\mathrm{lc}(1)}_{1,5/2,x,y} = -J - \frac{16J_a}{15} - \frac{J_b}{2} \mp \frac{J_d}{2} \pm \frac{16J_e}{5}, \tag{59}$$

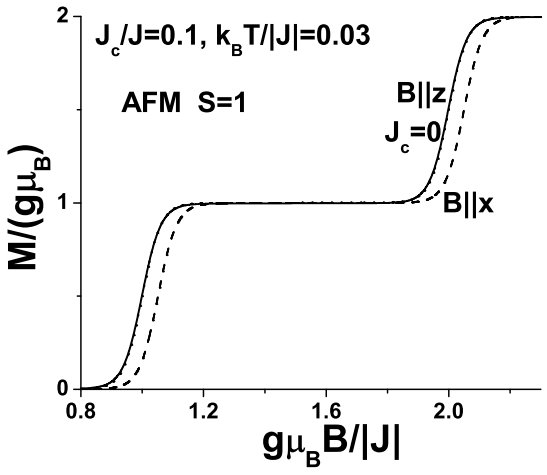


FIG. 14: Plot at $k_BT/|J| = 0.03$ and $J_c/J = 0.1$ of M/γ versus $\gamma B/|J|$ for the AFM spin 1 dimer. Curves for $\boldsymbol{B}||\hat{\boldsymbol{z}}$ (solid), $\boldsymbol{B}||\hat{\boldsymbol{x}}$ (dashed), and the isotropic case ($J_c = 0$, dotted) are shown.

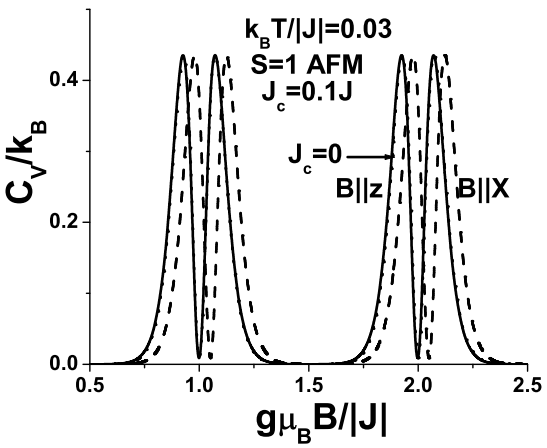


FIG. 15: Plot at $k_BT/|J| = 0.03$ and $J_c/J = 0.1$ of C_V/k_B versus $\gamma B/|J|$ for the AFM spin 1 dimer. Curves for $\boldsymbol{B}||\hat{\boldsymbol{z}}$ (solid), $\boldsymbol{B}||\hat{\boldsymbol{x}}$ (dashed), and the isotropic case ($J_b = 0$, dotted) are shown.

$$\gamma B^{\rm lc(1)}_{2,5/2,z} = -2J - \frac{8J_a}{35} - 3J_b, \quad (60)$$

$$\gamma B^{\rm lc(1)}_{2,5/2,x,y} = -2J + \frac{4J_a}{35} - \frac{J_b}{2} \mp \frac{5J_d}{2} \mp \frac{12J_e}{35}, \quad (61)$$

$$\gamma B^{\rm lc(1)}_{3,5/2,z} = -3J - \frac{106J_a}{63} - 5J_b, \quad (62)$$

$$\gamma B^{\rm lc(1)}_{3,5/2,x,y} = -3J + \frac{53J_a}{63} - \frac{J_b}{2} \mp \frac{9J_d}{2} \mp \frac{53J_e}{21}. \quad (63)$$

In Figs. 16-23, we plot M/γ and C_V/k_B versus $\gamma B/|J|$ for four low-T cases of AFM $s_1 = 5/2$ dimers, $J_b = 0.1J$, $J_d = 0.1J$, $J_a = 0.1J$, and $J_c = 0.1J$, respectively, and

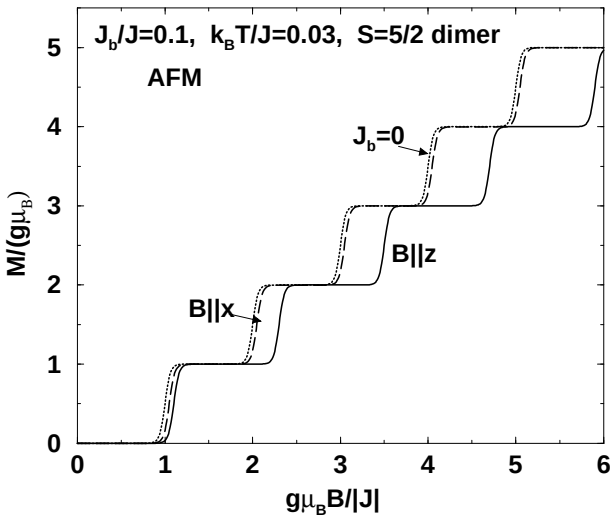


FIG. 16: Plot at $k_BT/|J| = 0.03$ of M/γ versus $\gamma B/|J|$ for the AFM spin 5/2 dimer with $J_b/J = 0.1$. $\boldsymbol{B}||\hat{\boldsymbol{z}}$ (solid), $\boldsymbol{B}||\hat{\boldsymbol{x}}$ (dashed), and the isotropic case ($J_b = 0$, dotted) are shown.

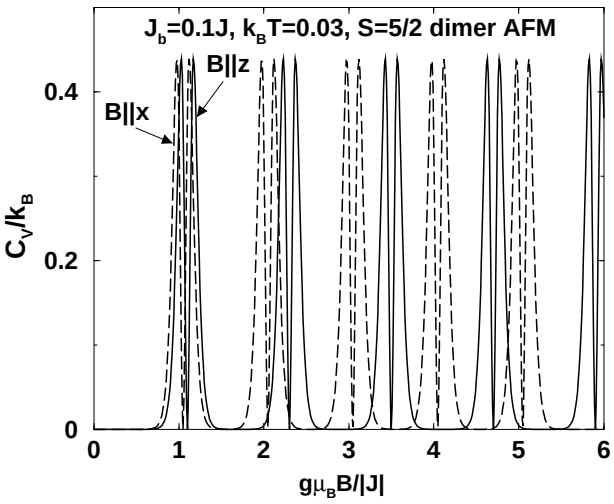


FIG. 17: Plot at $k_BT/|J| = 0.03$ and $J_b/J = 0.1$ of C_V/k_B versus $\gamma B/|J|$ for the AFM spin 5/2 dimer. Curves for $\boldsymbol{B}||\hat{\boldsymbol{z}}$ (solid), $\boldsymbol{B}||\hat{\boldsymbol{x}}$ (dashed), and the isotropic case ($J_b = 0$, dotted) are shown.

the other $J_j = 0$, taking $k_BT/|J| = 0.03$. In Fig. 24, examples of $M(\theta)$ at fixed B and $\phi = 0$ are shown. Figures 16-24 are sufficient to distinguish the more interesting local spin anisotropy effects in AFM dimers with higher s_1 values from the non-existent or less interesting ones present with $s_1 = 1/2, 1$, respectively. In Figs. 16, 18, 20, and 22, the solid and dashed curves represent the cases of $\boldsymbol{B}||\hat{\boldsymbol{z}}$ and $\boldsymbol{B}||\hat{\boldsymbol{x}}$, and the dotted curve is the isotropic case, $J_j = 0 \forall j$, as in Figs. 2-15. Because of the number of peaks in the specific heat curves, in Figs. 17, 19, 21, and 23, we ol=nly showed C_V/k_B versus $\gamma B/|J|$ for $\boldsymbol{B}||\hat{\boldsymbol{z}}$ (solid) and $\boldsymbol{B}||\hat{\boldsymbol{x}}$ (dashed). The isotropic curve with $J_j = 0$ $L\forall j$ was published previously.[14] That curve has

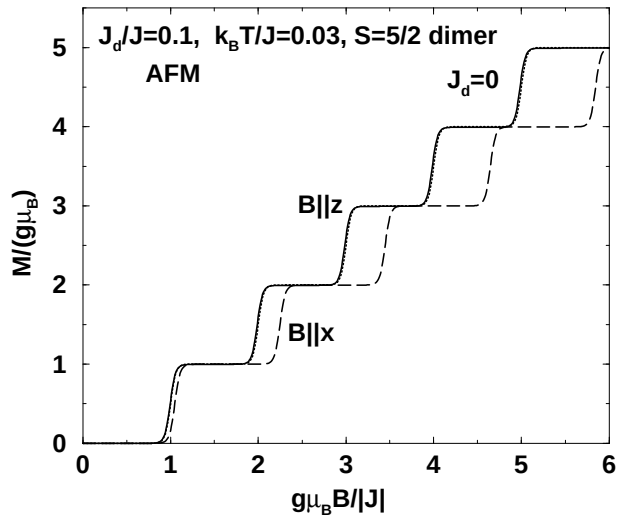


FIG. 18: Plot of M/γ versus $\gamma B/|J|$ for the AFM spin 5/2 dimer at $k_BT/|J| = 0.03$ with $J_d/J = 0.1$. Curves for $\boldsymbol{B}||\hat{\boldsymbol{z}}$ (solid), $\boldsymbol{B}||\hat{\boldsymbol{x}}$ (dashed), and the isotropic case ($J_b = 0$, dotted) are shown.

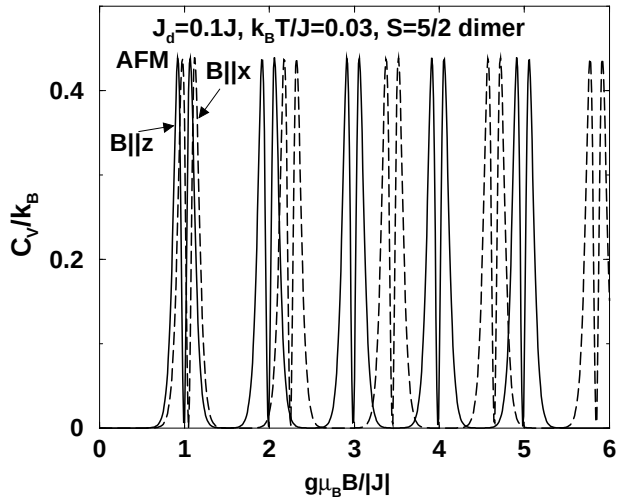


FIG. 19: Plot at $k_BT/|J| = 0.03$ and $J_d/J = 0.1$ of C_V/k_B versus $\gamma B/|J|$ at $k_BT/|J| = 0.03$ for the AFM spin 5/2 dimer. Curves for $\boldsymbol{B}||\hat{\boldsymbol{z}}$ (solid), $\boldsymbol{B}||\hat{\boldsymbol{x}}$ (dashed), and the isotropic case ($J_b = 0$, dotted) are shown.

minima at $\gamma B/|J| = s$ for $s = 1, \ldots, 5$, each of which is central to double peaks. $\mathcal{H}_a$ and $\mathcal{H}_b$ are invariant under $x \leftrightarrow y$, so curves for $\boldsymbol{B}||\hat{\boldsymbol{x}}$ in Figs. 16, 17, 20, and 21 are identical to those for $\boldsymbol{B}||\hat{\boldsymbol{y}}$. Since $\mathcal{H}_d$ and $\mathcal{H}_c$ are odd under $x \leftrightarrow y$, the $\boldsymbol{B}||\hat{\boldsymbol{x}}$ curves in Figs. 18, 19, 22, and 23 correspond to $\boldsymbol{B}||\hat{\boldsymbol{y}}$ with $J_d/J = -0.1J$, $J_c/J = -0.1$, respectively.

We first examine the global spin anisotropy effects of $\mathcal{H}_b$ and $\mathcal{H}_d$ in Figs. 16-19. These figures exhibit the same behavior shown for $s_1 = 1/2, 1$ in the corresponding Figs. 2-9. Note that $B^{\rm lc}_{s,5/2}(\theta, 0)$ is largest for $\theta = \pi/2$ with $J_b = 0.1J$ and for $\theta = 0$ with $J_d = 0.1J$, and increases monotonically with s, as for $s_1 = 1$ in both cases, nearly quantitatively consistent with Eqs. (58)-(63). By contrast, $B^{\rm lc}_{s,52}(\theta, 0)$ for $\theta = \pi/2$ with $J_b = 0.1J$ and for $\theta = 0$ for $J_d = 0.1J$ are nearly indistinguishable from the isotropic case, also nearly quantitatively consistent with Eqs. (58)-(63).

In contrast, the local field anisotropy interactions show very different and much more interesting behaviors. In Figs. 20-21, we present our results for the effects of the single-ion axial anisotropy interaction $\mathcal{H}_a$, Eq. (5). As in Fig. 10 for $s_1 = 1$, $B^{\rm lc}_{s,5/2}(\theta, 0) + sJ$ changes sign with increasing s. $B^{\rm lc}_{1,5/2}(0, 0) + J < 0$, whereas for $s \geq 2$, $B^{\rm lc}_{s,5/2}(0, 0) + sJ > 0$ and increases monotonically with s. For $\theta = \pi/2$, nearly the opposite situation occurs. $B^{\rm lc}_{s,5/2}(\pi/2, 0) + sJ$ is positive for $s = 1$ and decreases monotonically with increasing s. In both cases,$|B^{\rm lc}_{s,5/2}(\theta, 0) + sJ|$ is a minimum for $s = 2$. These local axial anisotropy effects, consistent with Eqs. (58)-(63), are very different than the global anisotropy ones pictured in Figs. 16-19. They are also much richer and interesting than the corresponding case for $s_1 = 1$ pictured in Figs. 10 and 11.

In Figs. 22-23, we present our M/γ versus $\gamma B/|J|$ results for the case of the local azimuthally anisotropic exchange interaction, $\mathcal{H}_c$, Eq. (8), evaluated for AFM dimers at $k_BT/|J| = 0.03$ with $J_c = 0.1J$ and the remaining $J_j = 0$. $B^{\rm lc(1)}_{s,5/2}$ for this case is obtained from Eqs. (58)-(63) by setting $J_d, J_e = \pm J_c/2$, respectively, and $J_a = J_b = 0$. $B^{\rm lc}_{s,5/2}(0, 0)$ is nearly indistinguishable from the isotropic case, as in Figs. 12 and 13 for $s_1 = 1$, except for some minor curve shape effects far from the step midpoints. $B^{\rm lc}_{s,5/2}(\pi/2, 0) + sJ$ is always positive, as for $s_1 = 1$ shown in Figs. 12 and 13, but has a minimum at $s = 3$. This is also in stark contrast to the monotonic global anisotropy behavior for $s_1 = 5/2$ seen in Figs. 16-19. Both of these behaviors are nearly quantitatively consistent with Eqs. (58)-(63) as modified to include J_c.

In contrast, the local field anisotropy interactions show very different behaviors. In Figs. 20 and 21, our results for the effects of the single-ion axial anisotropy interaction $\mathcal{H}_a$, Eq. (5), are shown. As in Figs. 10 and 11, the induction anisotropy effects of $\mathcal{H}_a$ change sign with increasing B. In Fig. 20, for $\boldsymbol{B}||\hat{\boldsymbol{z}}$ the first magnetization step appears at a lower value of $|\boldsymbol{B}|$ than in the isotropic case, and for steps 3-5, there is a monotonic increase in the extra field required for each step. The opposite is true for $\boldsymbol{B}||\hat{\boldsymbol{x}}$, for which the first step appears at a larger $|\boldsymbol{B}|$ value than for the isotropic case, and subsequent magnetization steps appear at monotonically decreasing values of $|\boldsymbol{B}|$. A cross-over occurs at about the second step, for which the effects of this type of anisotropy are small. The corresponding shifts in the positions of the double peaks in the specific heat are shown in Fig. 21. These local axial anisotropy effects are very different than the global anisotropy ones pictured in Figs. 16-19.

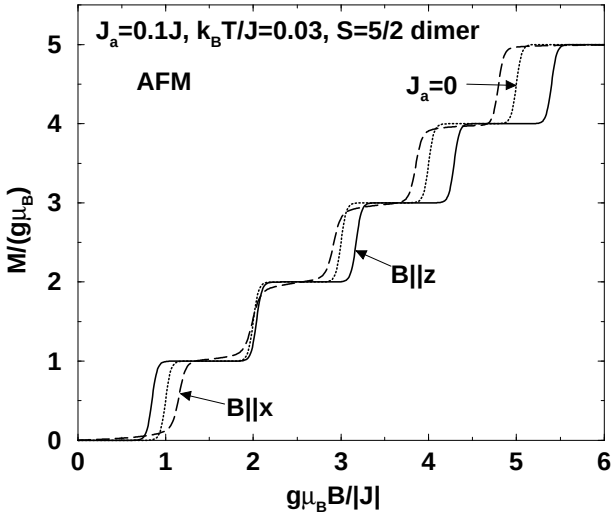


FIG. 20: Plot at $k_BT/|J| = 0.03$ and $J_a/J = 0.1$ of M/γ versus $\gamma B/|J|$ for the AFM spin 5/2 dimer. Curves for $\boldsymbol{B}||\hat{\boldsymbol{z}}$ (solid), $\boldsymbol{B}||\hat{\boldsymbol{x}}$ (dashed), and the isotropic case ($J_a = 0$, dotted) are shown.

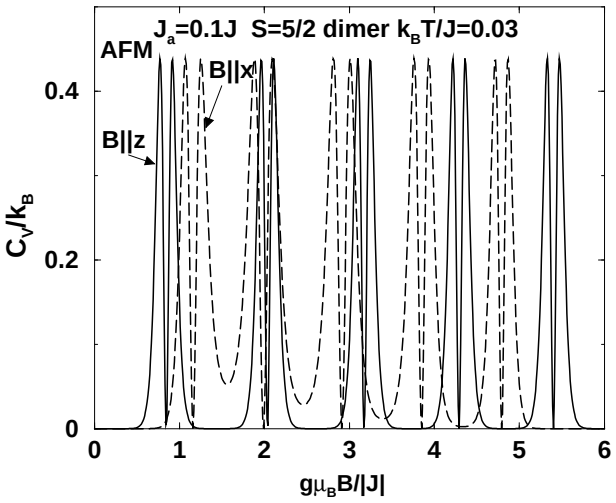


FIG. 21: Plot at $k_BT/|J| = 0.03$ and $J_a/J = 0.1$ of C_V/k_B versus $\gamma B/|J|$ at $k_BT/|J| = 0.03$ for the AFM spin 5/2 dimer. Curves for $\boldsymbol{B}||\hat{\boldsymbol{z}}$ (solid), $\boldsymbol{B}||\hat{\boldsymbol{x}}$ (dashed), and the isotropic case ($J_b = 0$, dotted) are shown.

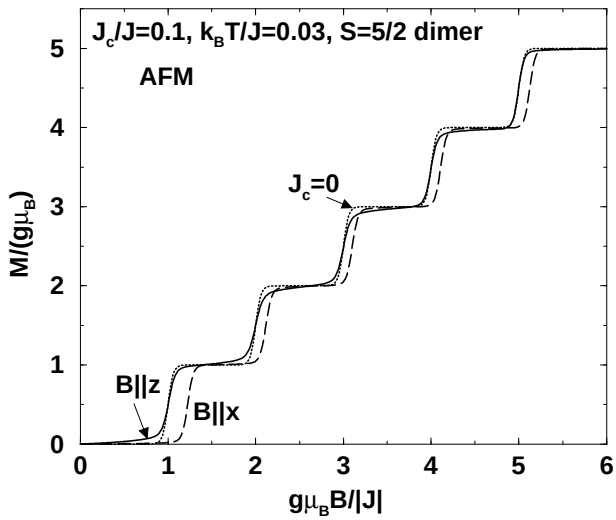


FIG. 22: Plot at $k_BT/|J| = 0.03$ of M/γ versus $\gamma B/|J|$ for the AFM spin 5/2 dimer with $J_c/J = 0.1$. $\boldsymbol{B}||\hat{\boldsymbol{z}}$ (solid), $\boldsymbol{B}||\hat{\boldsymbol{x}}$ (dashed), and the isotropic case ($J_b = 0$, dotted) are shown.

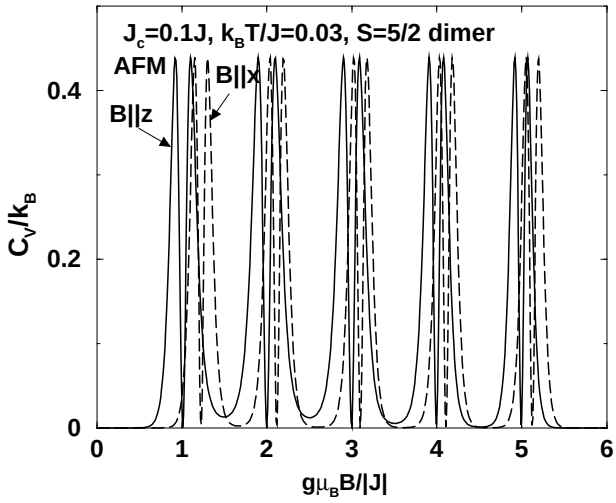


FIG. 23: Plot at $k_BT/|J| = 0.03$ and $J_c/J = 0.1$ of C_V/k_B versus $\gamma B/|J|$ at $k_BT/|J| = 0.03$ for the AFM spin 5/2 dimer. Curves for $\boldsymbol{B}||\hat{\boldsymbol{z}}$ (solid), $\boldsymbol{B}||\hat{\boldsymbol{x}}$ (dashed), and the isotropic case ($J_b = 0$, dotted) are shown.

In Figs. 22 and 23, we present our $\boldsymbol{M}$ and C_V results for the case of the local azimuthally anisotropic exchange interaction, $\mathcal{H}_c$, Eq. (8), evaluated for AFM dimers at $k_BT/|J| = 0.03$ with $J_c = 0.1J$, or equivalently with $J_d = 0.05J$ and $J_e = -0.05J$ (and the remaining $J_j = 0$). For $\boldsymbol{B}||\hat{\boldsymbol{z}}$, there is almost no change from the isotropic case, as occurred with the global azimuthal anisotropy pictured in Figs. 128 and 19. For $\boldsymbol{B}||\hat{\boldsymbol{x}}$, the field required for each step is larger than in the isotropic interaction case, as in Figs. 14 and 15 for $s_1 = 1$, and for global azimuthal anisotropy shown in Figs. 18 and 19. However, in this case, the extra induction required for each level crossing is non-monotonic in the crossing number, with the largest extra induction required for the first crossing, and the minimum extra induction required for the intermediate, third crossing. This is in stark contrast to the monotonic global anisotropy behavior for $s_1 = 5/2$ seen in Figs. 16-19. Although not pictured explicitly, the behavior for $J_e = 0.1J$ with the other $J_j = 0$ is rather like that of the $J_a = 0.1J$ curves pictured in Figs. 20 and 21 with $\hat{\boldsymbol{x}} \leftrightarrow \hat{\boldsymbol{z}}$, differing in ways similar to those differences between the $J_a = 0.1J$ and $J_e = 0.1J$ curves pictured for $s_1 = 1$ in Figs. 10-13.

Although not pictured explicitly, the behavior for $J_e =$

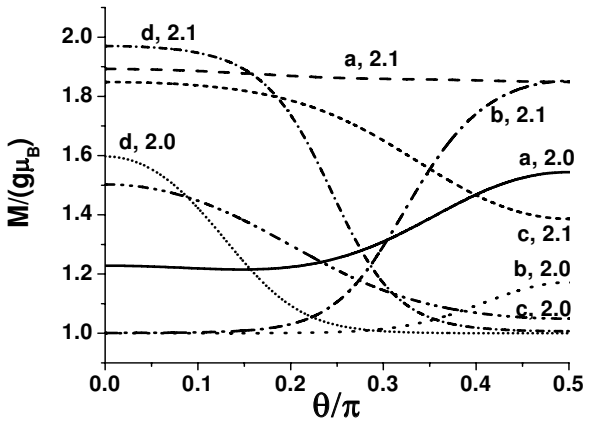


FIG. 24: Plot of M/γ at $\phi = 0$ versus θ/π near the second step at $\gamma B/|J| = 2.0, 2.1$ and $k_BT/|J| = 0.03$ for each $J_j/J = 0.1$ with $i = a, b, c, d$. Curves are labelled with $j, \gamma B/|J|$ values.

$0.1J$ with the other $J_j = 0$ is rather like that of the $J_a = 0.1J$ curves pictured in Figs. 20 and 21 with $\hat{\boldsymbol{z}} \leftrightarrow \hat{\boldsymbol{x}}$, differing in ways similar to those differences between the $J_a = 0.1J$ and $J_e = 0.1J$ curves pictured for $s_1 = 1$ in Figs. 10-13. As indicated in Eqs. (58)-(63), the $B^{\rm lc}_{s,5/2}(0,0)$ are nearly independent of J_e. However, the $B^{\rm lc}_{s,5/2}(\pi/2,0)+sJ$ with $J_e = 0.1J$ are nearly three times as large as for $J_a = 0.1J$ case, so that the minimum $|B^{\rm lc}_{s,5/2}(\pi/2,0) + sJ|$ is also a minimum for $s = 2$. More details are given in Section VII and Appendix D.

In addition, the angular dependencies of $\boldsymbol{M}$ are different for each of the four J_j we presented for $s_1 = 5/2$. In Fig. 24, we present the results for $|\boldsymbol{M}(B,\theta,\phi = 0)|/\gamma$ versus θ/π near the second level crossing at $\gamma|\boldsymbol{B}/J| = 2.0, 2.1$ and $k_BT/|J| = 0.03$ for each of the four $s_1 = 5/2$ AFM magnetization cases pictured in Figs. 16, 18, 20, and 22. Note that $|\boldsymbol{M}|(B,\pi-\theta,0)| = |\boldsymbol{M}(B,\theta,0)|$. The J_a and J_b curves, while rather similar at $\gamma|\boldsymbol{B}/J| = 2.0$, are very different at $\gamma|\boldsymbol{B}/J| = 2.1$. Hence, $\boldsymbol{M}(\boldsymbol{B})$ depends strongly upon the particular type of spin anisotropy.

ANALYTIC RESULTS FOR WEAKLY ANISOTROPIC DIMERS OF ARBITRARY SPIN

Induction representation eigenstates first order in the anisotropies

Since the diagonalization of the Hamiltonian matrix is difficult for an arbitrary magnetic field $\boldsymbol{H}$ direction and for an arbitrary combination of spin anisotropy interactions, and must be done for each value of s_1 separately, it is useful to consider a perturbative solution in the relative strengths J_j/J of the the anisotropy interactions. We nominally assume $|J_j/J| \ll 1$ for $j = a, b, d, e$. However, to compare with low-T $\boldsymbol{M}(\boldsymbol{B})$ and $C_V(\boldsymbol{B})$ experiments at various $\boldsymbol{H}$ directions and magnitudes, one cannot take B to be small. In order to incorporate an arbitrary $\boldsymbol{B}$ accurately, we rotate the crystal axes $(\hat{\boldsymbol{x}}, \hat{\boldsymbol{y}}, \hat{\boldsymbol{z}})$ to $(\hat{\boldsymbol{x}}', \hat{\boldsymbol{y}}', \hat{\boldsymbol{z}}')$, so that $\boldsymbol{B} = B\hat{\boldsymbol{z}}'$. The rotation matrix and a brief discussion of its ramifications are given in Appendix B.

In these rotated coordinates, the Zeeman interaction $-\gamma B S_{z'}$ is diagonal. We therefore denote this representation as the induction representation. The Hamiltonian $\mathcal{H}'$ in this representation is given in Appendix B. In the induction representation, we choose the quantum states to be $|\varphi^m_s\rangle$. In the absence of the four anisotropy interactions J_j, $\mathcal{H}' = \mathcal{H}'_0$ is diagonal,

$$\mathcal{H}'_0|\varphi^m_s\rangle \;=\; E^{m,(0)}_s|\varphi^m_s\rangle, \tag{64}$$

where

$$E^{m,(0)}_s \;=\; -Js(s+1)/2 - \gamma Bm. \tag{65}$$

The operations of the remaining terms in $\mathcal{H}'$ on the eigenstates $|\varphi^m_s\rangle$ are given in Appendix C. The first order correction to the energy in this representation is $E^{m,(1)}_s = \langle\varphi^m_s|\mathcal{H}'|\varphi^m_s\rangle$, which is found to be

$$\begin{aligned} E^{m,(1)}_{s,s_1} \;=\; & -\frac{J_b}{2}[2s(s+1)-1] - \frac{J_a}{2}[s(s+1)-1] \\ & + \frac{\tilde{J}^{s,s_1}_{b,a}}{2}[m^2 + s(s+1) - 1] \\ & + \frac{1}{2}[s(s+1) - 3m^2] \\ & \times\Big(\tilde{J}^{s,s_1}_{b,a}\cos^2\theta + \tilde{J}^{s,s_1}_{d,e}\sin^2\theta\cos(2\phi)\Big), \end{aligned} \tag{66}$$

where

$$\tilde{J}^{s,s_1}_{b,a} \;=\; J_b + \alpha_{s,s_1}J_a, \tag{67}$$

$$\tilde{J}^{s,s_1}_{d,e} \;=\; J_d + \alpha_{s,s_1}J_e, \tag{68}$$

and α_{s,s_1} is given by Eq. (29).

Since the θ,ϕ dependence of $E^{m,(1)}_s$ arises from the term proportional to $\tilde{J}^{s,s_1}_{b,a}\cos^2\theta + \tilde{J}^{s,s_1}_{d,e}\sin^2\theta\cos(2\phi)$, it is tempting to think that the thermodynamics with $\tilde{J}^{s,s_1}_{d,e} = 0$ and $\boldsymbol{B}||\hat{\boldsymbol{z}}$ are equivalent to those with $\tilde{J}^{s,s_1}_{b,a} = 0$ and $\boldsymbol{B}||\hat{\boldsymbol{x}}$. However, as shown explicitly in the following, the θ,ϕ-independent parts of Eq. (66) strongly break this apparent equivalence, causing the $B^{\rm lc}_{s,s_1}(\theta,\phi)$ for those two cases to differ. This implies that J_b and J_d are inequivalent, as are J_a and J_e, even to first order in the anisotropy strengths.

First order thermodynamics

To first order in the anisotropy interactions, s and m are still good quantum numbers, so the partition function

$$Z \;\approx\; \sum_{s=0}^{2s_1}\sum_{m=-s}^{s} e^{-\beta E^m_{s,s_1}}, \tag{69}$$

where $E^m_{s,s_1} = E^{m,(0)}_s + E^{m,(1)}_{s,s_1}$. Although it is difficult to perform the summation over the m values analytically, it is nevertheless elementary to evaluate Z numerically for an arbitrary B, θ, ϕ, and T from the eigenstate energies. The magnetization is obtained from

$$M(B,\theta,\phi) \approx \frac{\gamma}{Z}\sum_{s=0}^{2s_1}\sum_{m=-s}^{s} m e^{-\beta E^m_{s,s_1}}. \quad (70)$$

Similarly, the specific heat to first order in the anisotropy interactions is found from

$$C_V(B,\theta,\phi) \approx \frac{k_B\beta^2}{Z^2}\Big[Z\sum_{s=0}^{2s_1}\sum_{m=-s}^{s}(E^m_{s,s_1})^2 e^{-\beta E^m_{s,s_1}} - \Big(\sum_{s=0}^{2s_1}\sum_{m=-s}^{s} E^m_{s,s_1} e^{-\beta E^m_{s,s_1}}\Big)^2\Big]. \quad (71)$$

As a test of the accuracy of this first-order calculation, we have compared the first-order and exact $M(B)$ obtained for the $s_1 = 5/2$ dimer with $J_d = 0.1J$ and $\boldsymbol{B}||\hat{\boldsymbol{z}}$ in Fig. 25. The corresponding comparison between the first-order and exact $C_V(B)$ is shown in Fig. 26. We see that the curves evaluated using the first-order and the exact expressions for M and C_V with $s_1 = 5/2$ are indistinguishable at $k_BT/|J| = 0.03$. The C_V curves are noticeably different at $k_BT/|J| = 0.1$ for $\gamma B/|J| < 0.4$, and at $k_BT/|J| = 0.3$, they are noticeably different for $\gamma B/|J| < 2.6$. Corresponding noticeable differences in the M curves at the same B values appear at T values roughly three times as high as in the C_V curves.

At very low T, $k_BT/|J| \ll 1$, the most important states in this perturbative scheme are the minima for each s value, E^s_{s,s_1}, which determine the first-order level crossings. As $T \to 0$, we can ignore all of the $m \neq s$ states in Eqs. (69)-(71).

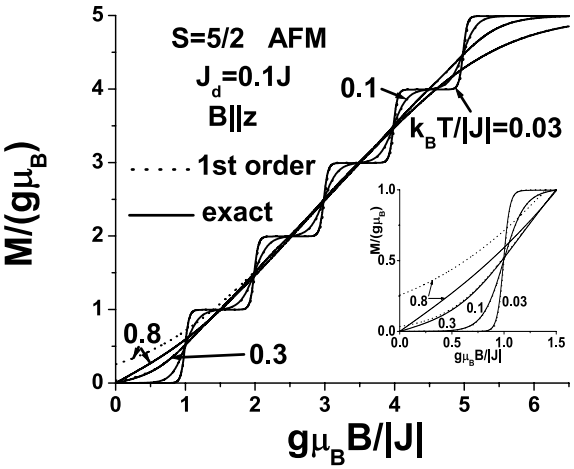


FIG. 25: Comparison of M/γ versus $\gamma B/|J|$ obtained using the first-order asymptotic form (dotted) with the exact calculation (solid), for the $s_1 = 5/2$ AFM dimer with $J_d = 0.1J$, $J_a = J_b = J_e = 0$, at $k_BT/|J| = 0.03, 0.1, 0.3, 0.8$, as indicated. Inset: expanded view of the region $0 \leq \gamma B/|J| \leq 1.5$.

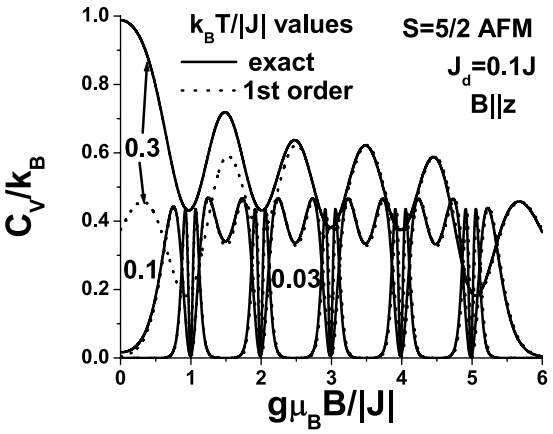


FIG. 26: Comparison of C_V/k_B versus $\gamma B/|J|$ obtained using the first-order asymptotic form (dotted) with the exact calculation (solid), for the $s_1 = 5/2$ AFM dimer with $J_d = 0.1J$, $J_a = J_b = J_e = 0$, at $k_BT/|J| = 0.03, 0.1, 0.3$, as indicated.

Level crossings first order in the anisotropies

We can find an expression for the $s^{\rm th}$ AFM level crossing at the induction $B^{\rm lc(1)}_{s,s_1}$ to first order in the anisotropy interactions for a general s_1 spin dimer by equating $E^{s,(0)}_s + E^{s,(1)}_{s,s_1}$ to $E^{s-1,(0)}_{s-1} + E^{s-1,(1)}_{s-1,s_1}$,

$$\gamma B^{\rm lc(1)}_{s,s_1} = -Js - J_b/2 - c_{s,s_1}J_a - \frac{(4s-3)}{2}[J_b\cos^2\theta + J_d\sin^2\theta\cos(2\phi)] + 3c_{s,s_1}[J_a\cos^2\theta + J_e\sin^2\theta\cos(2\phi)], \quad (72)$$

$$c_{s,s_1} = \frac{[3+3s-5s^2-4s^3+4s_1(s_1+1)]}{2(2s+1)(2s+3)}. \quad (73)$$

This expression is consistent with those obtained for $s_1 = 1/2, 1$ given by Eqs. (52) and (54)-(57). In addition, this expression is nearly quantitatively in agreement with the $M(B)$ and $C_V(B)$ behaviors pictured for $s_1 = 5/2$ in Figs. 16-23. We note that $\gamma B^{\rm lc(1)}_{s,s_1}$ contains the θ, ϕ-independent terms, $-Js - J_b/2 - c_{s,s_1}J_a$, which distinguish J_b from J_d and J_a from J_e.

In particular, we note that the single-ion anisotropy interactions behave very differently with increasing step number than do the global anisotropy interactions, especially for large s_1. For the three cases we studied in detail, for $s_1 = 1/2$, $c_{1,1/2} = 0$, so that the local anisotropy terms are irrelevant, for $s_1 = 1$, $c_{1,1} = \frac{1}{6}$ and $c_{2,1} = -\frac{1}{2}$ have different signs, and for $s_1 = 5/2$ as in Fe_2 dimers, the

first three $c_{s,5/2}$ coefficients are $\frac{16}{15}$, $-\frac{4}{35}$, and $-\frac{53}{63}$, respectively, the second being an order of magnitude smaller than the other two, and opposite in sign from the first. For $s_1 = 9/2$ dimers such as $[Mn_4]_2$, the first four $c_{s,9/2}$ are $\frac{16}{5}$, $\frac{4}{5}$, $-\frac{1}{3}$, and $-\frac{37}{33}$, which changes sign between $s = 2$ and $s = 3$, where its magnitude is a minimum.

This is in sharp contrast to the global anisotropy interactions, for which the analogous coefficient $(4s-3)/2$ increases monotonically from $\frac{1}{2}$ to $\frac{5}{2}$ as s increases from 1 to 2, independent of s_1. These differences should be possible to verify experimentally in careful low-T experiments at high magnetic fields applied at various directions on single crystals of those $s_1 = 5/2$ Fe_2 and $s_1 = 9/2$ $[Mn_4]_2$ dimers for which $|J|$ is sufficiently small.

Level crossings to second order in the anisotropy energies

To aid in the analysis of experimental data, we have extended this perturbative calculation to second order. Since we expect the $|J_j/J| \leq 0.1$ in most circumstances, this extension ought to be sufficient to accurately analyze most experimentally important samples. To second order in the anisotropy interactions, the eigenstate energies $E^{m,(2)}_{s,s_1}$ are given in Appendix C. We note that the $E^{m(2)}_{s,s_1}$ contains divergences at $\gamma B/|J| = 0, 2s-1, 2s+3, s-1/2$, and $s+3/2$, so that near to those values, one would need to modify the perturbation expansion to take proper account of the degeneracies. Hence, the expressions for $E^{m(2)}_{s,s_1}$ cannot be used in the asymptotic expressions for the thermodynamics, Eqs. (69)-(71). However, as the sth AFM level crossing occurs approximately at $\gamma B/|J| = s$, which is far from any divergences, we can safely use this second order expansion to obtain an expression for the level crossings second order in the anisotropy interaction energies. We find

$$\gamma B^{\rm lc(2)}_{s,s_1} \;=\; \gamma B^{\rm lc(1)}_{s,s_1} + \left(E^{s,(2)}_{s,s_1} - E^{s-1,(2)}_{s-1,s_1}\right)\Big|_{B=-Js/\gamma}, \tag{74}$$

where $\gamma B^{\rm lc(1)}_{s,s_1}$ is given by Eq. (73).

The full expression for $B^{\rm lc(2)}_{s,s_1}$ is given in Appendix D. From this expression, it is easy to see that for $s_1 = 1/2$, $E^{\rm lc(2)}_{1,1/2} = \frac{1}{2}f_1(\theta,\phi) + \frac{1}{8}f_4(\theta,\phi)$, where f_1 and f_4 are given in Appendix D. For $\boldsymbol{B}||\hat{\boldsymbol{z}}$, $E^{\rm lc(2)}_{1,1/2} = -\frac{1}{2}J_d^2/|J|$, and with $\boldsymbol{B}||\hat{\boldsymbol{x}},\hat{\boldsymbol{y}}$, $E^{\rm lc(2)}_{1,1/2} = -\frac{1}{8}(J_b \pm J_d)^2/|J|$, in agreement with the expansion to second order in the J_j of our exact formulas in Eq. (52). However, the second order functions have more complicated θ,ϕ dependencies than do the first order $B^{\rm lc(1)}_{s,s_1}$ in Eq. (73). We have also explicitly checked each formula in Appendix D for $s_1 = 1$ and $s = 1, 2$. Thus, Eq. (74) is a highly accurate expression for the full θ,ϕ dependencies of all $s = 1,\ldots,2s_1+1$ level crossings of a single crystal dimer of single ion spin s_1.

By superposing this non-universal level-crossing formula, Eq. (74), combined with the universal behavior presented in Eqs. (**??**)-(40), it is easy to use our results in accurate fits to experimental data at low temperatures and high magnetic fields on dimers with arbitrary s_1 values.

SUMMARY AND CONCLUSIONS

In summary, we solved for the low-temperature magnetization and specific heat of equal spin s_1 antiferromagnetic dimer single molecule magnets, including the most general forms of anisotropic spin exchange interactions quadratic in the spin operators. The magnetization and specific heat exhibit steps and zeroes, respectively, at the non-universal level-crossing induction values $B^{\rm lc}_{s,s_1}(\theta,\phi)$, but the magnetization steps and their midpoint slopes, plus the two peaks surrounding the specific heat zeroes all exhibit universal behavior at sufficiently low temperatures. Local (or single-ion) anisotropy interactions lead to low-temperature magnetization step plateaus that have a much richer variation with the magnetic induction $\boldsymbol{B}$ than do those obtained from global anisotropy interactions, provided that $s_1 > 1/2$. We derived simple, accurate asymptotic analytic expressions for the low-temperature magnetization and specific heat for the most general quadratic anisotropic spin interactions at an arbitrary $\boldsymbol{B}$, and an accurate expression for $B^{\rm lc}_{s,s_1}(\theta,\phi)$, enabling fast and accurate fits to experimental data.

There were two low-T $M(B)$ studies of Fe_2 dimers.[16, 17] For μ-oxalatotetrakis(acetylacetonato)Fe_2, all five peaks in dM/dH were measured in pulsed magnetic fields H. These evenly spaced peaks indicated little, if any, spin anisotropy effects.[16] On the other hand, studies of the first 2-3 dM/dH peaks in powdered samples of $[Fe(salen)Cl]_2$, where salen is N,N'-ethylenebis(salicylideneiminato), were much more interesting.[17] These data showed a broad first peak at $B = 17 - 20$T that was only partially resolvable into two separate peaks, followed by a sharp second peak at $B = 36$ T, consistent with local axial anisotropy of strength $|J_a/J| \approx 0.1$, as obtained from the derivatives of the curves shown in Fig. 20 From Eqs. (58)-(63), one could also have $|(J_a \pm 3J_3)/J| \approx 0.1$. These values might perhaps be combined with a smaller $|J_c/J|$, obtained from the derivatives of the curves pictured in Fig. 22.

Without a detailed single crystal study with the magnetic field directed along a number of different crystal directions, it is impossible to determine the relative amounts of J_a and J_e that would best fit the data. However, the existing data on $[Fe(salen)Cl]_2$ appear to be

inconsistent with a predominant global anisotropy interaction of either type, as obtained from the derivatives of the curves shown in Figs. 16 and 18. Only single crystal studies could determine if a small amount of such global anisotropy interactions were present in addition to one or more presumably larger local spin anisotropy interactions. In comparing the two materials cited above, it appears that the interaction of a Cl^- ion neighboring each Fe^{3+} ion leads to strong local (or single-ion) anisotropy effects. In order to verify this hypothesis and to elucidate the details of the interactions, further experiments using single crystals in different field orientations on this and related Fe_2 dimers with 1-3 similarly bonded Cl^- ions are urged.[19, 20] We also urge single crystal data on some of the $s_1 - 9/2$ $[Mn_4]_2$ dimers,[21, 22] as well as on $s_1 = 1/2$ dimers lacking in predicted local spin anisotropy effects. [11–14] To aid in the fits, we derived simple, useful formulas for the magnetization and specific heat at low temperature and sufficiently large magnetic induction, and accurate formulas for the level crossing inductions.

With local anisotropy interactions, the total spin s is not a good quantum number, potentially modifying our understanding of quantum tunneling processes. It might also be possible to fit a variety of experimental results using a smaller, consistent set of model parameters.[6] We emphasize that the study of SMM dimers, for which the most general anisotropic quadratic exchange interactions can be solved exactly, may be our best hope for attaining a more fundamental understanding of the underlying physics of single molecule magnets.

ACKNOWLEDGMENTS

We thank the Max-Planck-Institut für Physik komplexer Systeme, Dresden, Germany, the University of North Dakota, Grand Forks, ND, USA, and Talat S. Rahman for their kind hospitality and support. This work was supported by the Netherlands Foundation for the Fundamental Research of Matter and by the NSF under contract NER-0304665.

APPENDIX A

Specific heat details for $s_1 = 1/2$

We first present the numerators of the exact expressions for the specific heat with $s_1 = 1/2$ and $\boldsymbol{B}||\hat{\boldsymbol{i}}$ for $i = x, y, z$. We have

$$\begin{aligned}\mathcal{N}_{x,y} &= F_{x,y}^2 + \frac{1}{4}(J+2J_{y,x})^2 e^{\beta[2(J_{y,x}-J_{x,y})-J]} \\ &\quad + F_{x,y}\sinh(\beta F_{x,y})e^{-\beta J_{x,y}} \\ &\quad \times[(J+J_{x,y})e^{-\beta J} + (J_{x,y}-2J_{y,x})e^{2\beta J_{y,x}}] \\ &\quad + \frac{1}{2}e^{-\beta J_{x,y}}\cosh(\beta F_{x,y}) \\ &\quad \times\Big([(J+J_{x,y})^2 + F_{x,y}^2]e^{-\beta J} \\ &\quad + [(2J_{y,x}-J_{x,y})^2 + F_{x,y}^2]e^{2\beta J_{y,x}}\Big), \qquad (75)\end{aligned}$$

$$\begin{aligned}\mathcal{N}_z &= F_z^2\cosh(2\beta F_z) + \frac{J^2}{4}e^{-\beta(J+2J_b)} \\ &\quad + \frac{1}{2}\cosh(\beta F_z)\Big(\Delta_z(J_b^2+F_z^2) \\ &\quad + e^{-\beta(J+J_b)}J(J+2J_b)\Big) \\ &\quad + F_z\sinh(\beta F_z)\Big(J_b\Delta_z + Je^{-\beta(J+J_b)}\Big). \qquad (76)\end{aligned}$$

Eigenvalues for $s_1 = 1$

In the remainder of this appendix, we provide the details of our exact results for $s_1 = 1$. The cubic equation for the three $s = 1$ eigenvalues is given by

$$\begin{aligned}\epsilon_n &= -J - J_b - J_a + \lambda_n, \text{ for } n = 2, 3, 4, \qquad (77)\\ 0 &= -\lambda_n^3 - (J_a - J_b)\lambda_n^2 + \lambda_n[b^2 + (J_d - J_e)^2] \\ &\quad + (J_a - J_b)[b_z^2 + (J_d - J_e)^2] \\ &\quad - (J_d - J_e)(b_x^2 - b_y^2), \qquad (78)\end{aligned}$$

where the $b_i = \gamma B_i$ as in Eq. (**??**). For $\boldsymbol{B}||\hat{\boldsymbol{z}}$, the cubic equation is easily solved to yield

$$\lambda_n = J_b - J_a, \pm\sqrt{b^2 + (J_d - J_e)^2}. \qquad (79)$$

For $\boldsymbol{B}||\hat{\boldsymbol{x}}, \hat{\boldsymbol{y}}$, we have

$$\lambda_n = \pm(J_e - J_d), -J_{y,x} \pm \sqrt{b^2 + \overline{J}_{x,y}^2}, \qquad (80)$$

$$\overline{J}_{x,y} = \frac{1}{2}[J_a - J_b \mp (J_d - J_e)], \qquad (81)$$

where $\overline{J}_x$ ($\overline{J}_y$) corresponds to the upper (lower) sign. The rank ordering of these eigenvalues depends upon B and the various anisotropy parameters, of course.

The six eigenvalues for the mixed $s = 0, 2$ states satisfy

$$\epsilon_n = -3J - \frac{4}{3}J_a - 2J_b + \lambda_n \qquad (82)$$

We then define

$$\tilde{J}_a = \frac{\sqrt{8}}{3}J_a, \qquad (83)$$

$$\tilde{J}_b = J_b + J_a/3, \qquad (84)$$

$$\tilde{J}_d = J_d + J_e/3, \qquad (85)$$

$$\tilde{J}_e = \frac{2}{\sqrt{3}}J_e, \qquad (86)$$

$$\tilde{J} = J - \frac{2}{9}J_a, \qquad (87)$$

and obtain the Hermitian matrix $\overleftrightarrow{\boldsymbol{M}}$ for the six $s=0,2$ states, the eigenvalues of which are the λ_n. For brevity, we let

$$\begin{aligned}
Q_n^p &= n\tilde{J}_b + pb\cos\theta, && (88)\\
b_\perp &= b\sin\theta e^{-i\phi}, && (89)\\
b_3 &= \sqrt{\frac{3}{2}}b_\perp, && (90)\\
a &= \tilde{J}_a, && (91)\\
d_3 &= 3\tilde{J}_d, && (92)\\
d_6 &= \sqrt{6}\tilde{J}_d, && (93)\\
e &= \tilde{J}_e. && (94)
\end{aligned}$$

Then, the matrix $\overleftrightarrow{\boldsymbol{M}}$ is given by

$$\overleftrightarrow{\boldsymbol{M}} = \begin{pmatrix}
Q_{-2}^{-2} & -b_\perp & -d_6 & 0 & 0 & -e \\
-b_\perp^* & Q_1^{-1} & -b_3 & -d_3 & 0 & 0 \\
-d_6 & -b_3^* & Q_2^0 & -b_3 & -d_6 & -a \\
0 & -d_3 & -b_3^* & Q_1^1 & -b_\perp & 0 \\
0 & 0 & -d_6 & -b_\perp^* & Q_{-2}^2 & -e \\
-e & 0 & -a & 0 & -e & Q_2^0+3\tilde{J}
\end{pmatrix}. \quad (95)$$

After some rearrangement, the λ_n are found to satisfy

$$\begin{aligned}
0 &= \sum_{p=0}^{6} c_p(\lambda_n)^p, && (96)\\
c_6 &= 1, && (97)\\
c_5 &= -2\tilde{J}_b - 3\tilde{J}, && (98)\\
c_4 &= -\tilde{J}_a^2 - 7\tilde{J}_b^2 - 21\tilde{J}_d^2 - 2\tilde{J}_e^2 - 5b^2, && (99)\\
c_3 &= 3\tilde{J}(7\tilde{J}_b^2 + 21\tilde{J}_d^2 + 5b^2)\\
&\quad +2\tilde{J}_b(-\tilde{J}_a^2 + 8\tilde{J}_b^2 + 12\tilde{J}_d^2 + 2\tilde{J}_e^2)\\
&\quad +4\sqrt{6}\tilde{J}_a\tilde{J}_d\tilde{J}_e + 21\tilde{J}_d(b_x^2 - b_y^2)\\
&\quad +3\tilde{J}_b(b^2 + 7b_z^2), && (100)\\
c_2 &= 3\tilde{J}\Big(\tilde{J}_b[-2\tilde{J}_b^2 + 18\tilde{J}_d^2 + 7(b^2 - 3b_z^2)]\\
&\quad -21\tilde{J}_d(b_x^2 - b_y^2)\Big)\\
&\quad +\tilde{J}_a^2(3\tilde{J}_b^2 + 9\tilde{J}_d^2 + 2b^2 + 3b_z^2)\\
&\quad +2\tilde{J}_b^2[4\tilde{J}_b^2 + 3\tilde{J}_e^2 + 11(b^2 - 3b_z^2)]\\
&\quad +2\tilde{J}_d^2[54(\tilde{J}_b^2 + \tilde{J}_d^2) + 9\tilde{J}_e^2 - 12(b^2 - 3b_z^2)]\\
&\quad +2\tilde{J}_e^2(4b^2 - 3b_z^2) + 4b^4\\
&\quad +2(3\tilde{J}_b\tilde{J}_d - \sqrt{6}\tilde{J}_a\tilde{J}_e)(b_x^2 - b_y^2), && (101)\\
c_1 &= -12\tilde{J}\Big(b^4 + 3\tilde{J}_b^4 + 18\tilde{J}_b^2\tilde{J}_d^2 + 27\tilde{J}_d^4\\
&\quad +2(\tilde{J}_b^2 - 3\tilde{J}_d^2)(b^2 - 3b_z^2)\\
&\quad +12\tilde{J}_b\tilde{J}_d(b_x^2 - b_y^2)\Big)\\
&\quad -2\tilde{J}_b\Big(2(9\tilde{J}_d^2 + b^2)(b^2 + 3b_z^2)\\
&\quad -\tilde{J}_a^2(b^2 - 3b_z^2) + 6\tilde{J}_b^2(b^2 - 5b_z^2)\\
&\quad +(42\tilde{J}_b\tilde{J}_d + \sqrt{6}\tilde{J}_a\tilde{J}_e)(b_x^2 - b_y^2)\\
&\quad -2\tilde{J}_a^2(\tilde{J}_b^2 + 9\tilde{J}_d^2) + 8\tilde{J}_b^2(2\tilde{J}_b^2 + 6\tilde{J}_d^2 + \tilde{J}_e^2)\\
&\quad +6\sqrt{6}\tilde{J}_a\tilde{J}_b\tilde{J}_d\tilde{J}_e\Big)\\
&\quad -2\tilde{J}_d\Big(6(b^2 - 3\tilde{J}_d^2 + \tilde{J}_e^2)(b_x^2 - b_y^2)\\
&\quad -\sqrt{6}\tilde{J}_a\tilde{J}_e(b^2 - 3b_z^2 - 18\tilde{J}_d^2)\Big), && (102)\\
c_0 &= -12\tilde{J}\Big(\tilde{J}_b b^2(b^2 - 3b_z^2)\\
&\quad -3\tilde{J}_d(b^2 - \tilde{J}_b^2 - 3\tilde{J}_d^2)(b_x^2 - b_y^2)\\
&\quad +\tilde{J}_b^3(b^2 + 3b_z^2 - 2\tilde{J}_b^2 + 12\tilde{J}_d^2)\\
&\quad -3\tilde{J}_b\tilde{J}_d^2(7b^2 - 3b_z^2 - 18\tilde{J}_d^2)\Big)\\
&\quad -\tilde{J}_a^2\Big((b^2 - 3b_z^2 + 2\tilde{J}_b^2)^2 + 36\tilde{J}_d^2(b_z^2 - \tilde{J}_b^2)\Big)\\
&\quad -4\tilde{J}_b^2\Big(2b^2(b^2 - 3b_z^2 + \tilde{J}_e^2) - 2\tilde{J}_b^2(2\tilde{J}_b^2 + \tilde{J}_e^2 - b^2 - 3b_z^2)\\
&\quad +6\tilde{J}_d^2(-7b^2 + 3b_z^2 + 4\tilde{J}_b^2 + 18\tilde{J}_d^2 + 3\tilde{J}_e^2)\\
&\quad +(6\tilde{J}_b\tilde{J}_d - \sqrt{6}\tilde{J}_a\tilde{J}_e)(b_x^2 - b_y^2)\Big)\\
&\quad +24\tilde{J}_b\tilde{J}_d(b_x^2 - b_y^2)(b^2 - 3\tilde{J}_d^2 - 2\tilde{J}_e^2)\\
&\quad +2\sqrt{6}\tilde{J}_a\tilde{J}_e(b_x^2 - b_y^2)(b^2 - 3b_z^2 - 6\tilde{J}_d^2)\\
&\quad -6\tilde{J}_e^2(b_x^2 - b_y^2)^2\\
&\quad +8\sqrt{6}\tilde{J}_a\tilde{J}_b\tilde{J}_d\tilde{J}_e(2b^2 - 3b_z^2 + \tilde{J}_b^2 - 9\tilde{J}_d^2). && (103)
\end{aligned}$$

$\boldsymbol{B}$ along a crystal axis

We recall that the six Hamiltonian matrix eigenvalues ϵ_n are generally given by Eq. (82). For the special case $\boldsymbol{B}||\hat{\boldsymbol{z}}$, $\overleftrightarrow{\boldsymbol{M}}$ is block diagonal. The resulting eigenvalues of the nominal $s=2, m=\pm1$ notation are

$$\lambda_{6,8}^z = \tilde{J}_b \mp \sqrt{b^2 + 9\tilde{J}_d^2}. \quad (104)$$

The remaining four states are obtained from

$$\begin{aligned}
0 &= \sum_{p=0}^{4} k_p^z(\lambda_n^z)^p, && (105)\\
k_4^z &= 1, && (106)\\
k_3^z &= -3\tilde{J}, && (107)\\
k_2^z &= -6\tilde{J}\tilde{J}_b - \tilde{J}_a^2 - 8\tilde{J}_b^2 - 12\tilde{J}_d^2 - 2\tilde{J}_e^2 - 4b^2, && (108)\\
k_1^z &= 12\tilde{J}(b^2 + \tilde{J}_b^2 + 3\tilde{J}_d^2)\\
&\quad +4\tilde{J}_b(4b^2 - \tilde{J}_a^2) + 4\sqrt{6}\tilde{J}_a\tilde{J}_d\tilde{J}_e, && (109)\\
k_0^z &= 24\tilde{J}\tilde{J}_b(-b^2 + \tilde{J}_b^2 + 3\tilde{J}_d^2) + 4\tilde{J}_a^2(b^2 - \tilde{J}_b^2)\\
&\quad +8\tilde{J}_b^2(-2b^2 + 2\tilde{J}_b^2 + 6\tilde{J}_d^2 + \tilde{J}_e^2)\\
&\quad +8\sqrt{6}\tilde{J}_a\tilde{J}_b\tilde{J}_d\tilde{J}_e. && (110)
\end{aligned}$$

Similarly, for $\boldsymbol{B}||\hat{\boldsymbol{x}}, \hat{\boldsymbol{y}}$, $\overleftrightarrow{\boldsymbol{M}}$ is also block diagonal. The resulting eigenvalues of the nominal $s=2, m=\pm1$ notation are

$$\lambda_{6,8}^{x,y} = \frac{3}{2}\tilde{J}_{x,y} - 2\tilde{J}_b \mp \sqrt{b^2 + \tilde{J}_{x,y}^2}, \quad (111)$$

$$\tilde{J}_{x,y} = \frac{3}{2}(\tilde{J}_b \pm \tilde{J}_d). \quad (112)$$

The remaining four states are obtained from

$$\begin{aligned}
0 &= \sum_{p=0}^{4} n_p^{x,y} (\lambda_n^{x,y})^p, && (113)\\
n_4^{x,y} &= 1, && (114)\\
n_3^{x,y} &= -3(\tilde{J} + \tilde{J}_b \mp \tilde{J}_d), && (115)\\
n_2^{x,y} &= -\tilde{J}_a^2 - 2\tilde{J}_b^2 - 12\tilde{J}_d^2 - 2\tilde{J}_e^2 + 3\tilde{J}\tilde{J}_b \\
&\quad -4b^2 \mp 3\tilde{J}_d(2\tilde{J}_b + 3\tilde{J}), && (116)\\
n_1^{x,y} &= 6\tilde{J}_e^2(\tilde{J}_b \mp \tilde{J}_d) + 4b^2(3\tilde{J} + \tilde{J}_b \pm 3\tilde{J}_d) \\
&\quad +12(\tilde{J}_b^2 + 3\tilde{J}_d^2)(\tilde{J} + \tilde{J}_b \mp \tilde{J}_d) \\
&\quad -\tilde{J}_a^2(\tilde{J}_b \pm 3\tilde{J}_d) + 4\sqrt{6}\tilde{J}_a\tilde{J}_d\tilde{J}_e, && (117)\\
n_0^{x,y} &= b^2[\tilde{J}_a^2 + 12\tilde{J}(\tilde{J}_b \mp 3\tilde{J}_d) + 8\tilde{J}_b^2 + 6\tilde{J}_e^2 \\
&\quad \mp 24\tilde{J}_b\tilde{J}_d \mp 2\sqrt{6}\tilde{J}_a\tilde{J}_e] \\
&\quad +2\tilde{J}_b^2[\tilde{J}_a^2 - 4\tilde{J}_b^2 - 6\tilde{J}\tilde{J}_b - 12\tilde{J}_d^2 - 2\tilde{J}_e^2] \\
&\quad \pm 12\tilde{J}_d(2\tilde{J}_b + 3\tilde{J})(\tilde{J}_b^2 + 3\tilde{J}_d^2) \\
&\quad \mp 6\tilde{J}_b\tilde{J}_d(\tilde{J}_a^2 \pm 6\tilde{J}\tilde{J}_d - 2\tilde{J}_e^2) \\
&\quad -4\sqrt{6}\tilde{J}_a\tilde{J}_d\tilde{J}_e(\tilde{J}_b \mp 3\tilde{J}_d). && (118)
\end{aligned}$$

Simple special cases

When only one of the $J_j \neq 0$, the eigenvalues for $\boldsymbol{B}||\hat{\boldsymbol{z}}$ simplify considerably. For $J_b \neq 0$, we have

$$\lambda_n^z = 3J + 2J_b, 2J_b, J_b \pm b, -2J_b \pm 2b. \quad (119)$$

For $J_d \neq 0$, we find

$$\lambda_n^z = 0, 3J, \pm\sqrt{b^2 + 9J_d^2}, \pm 2\sqrt{b^2 + 3J_d^2}. \quad (120)$$

For $J_a \neq 0$, the eigenvalues can also be found analytically,

$$\lambda_n^z = -\frac{2J_a}{3} \pm 2b, \frac{J_a}{3} \pm b, \frac{J_a}{3} + \frac{3J}{2} \pm \sqrt{\frac{9}{4}J^2 + J_a^2 - JJ_a}. \quad (121)$$

We note that the ground state energy in this case is

$$E_1 = -\frac{3}{2}J - J_a - \sqrt{\frac{9}{4}J^2 + J_a^2 - JJ_a}, \quad (122)$$

which explicitly involves mixing of the $s = m = 0$ and the $s = 2, m = 0$ states. For $J_e \neq 0$, three of the eigenvalues are

$$\lambda_n^z = 0, \pm\sqrt{b^2 + J_e^2}, \quad (123)$$

$$(124)$$

and the remaining three satisfy the cubic equation,

$$0 = x^3 - 3Jx^2 - 4x(b^2 + J_e^2) + 4J(J_e^2 + 3b^2). \quad (125)$$

We note that the cubic equation must be solved to obtain the ground state energy, since the $s = m = 0$ state mixes with the $s = 2, \pm 2$ states. For $\boldsymbol{B}||\hat{\boldsymbol{x}}, \hat{\boldsymbol{y}}$, with $J_b \neq 0, J_d \neq 0$, the eigenvalues are

$$\lambda_n^{x,y} = 3J + 2J_b, -2J_b + \tilde{J}_{x,y} \pm \sqrt{b^2 + \tilde{J}_{x,y}^2}, \quad (126)$$

where $\tilde{J}_{x,y}$ is given by Eq. (112), and the other three eigenvalues satisfy the cubic equation,

$$\begin{aligned}
0 &= -x^3 + (J_b \mp 3J_d)x^2 + 4(b^2 + J_b^2 + 3J_d^2)x \\
&\quad +4(b^2 - J_b^2 - 3J_d^2)(J_b \mp 3J_d). && (127)
\end{aligned}$$

For $J_a \neq 0$, two of the eigenvalues satisfy

$$\lambda_n^{x,y} = -\frac{J_a}{6} \pm \sqrt{b^2 + J_a^2/4}, \quad (128)$$

and the other four eigenvalues satisfy the quartic equation,

$$\begin{aligned}
0 &= 81x^4 - 27(J_a + 9J)x^3 - 9(36b^2 - 9JJ_a + 12J_a^2)x^2 \\
&\quad +12(-J_a^3 + 9JJ_a^2 - 9b^2J_a + 81b^2J)x \\
&\quad +4(4J_a^4 - 9JJ_a^3 + 18b^2J_a^2 + 81b^2JJ_a). && (129)
\end{aligned}$$

Finally, for $J_e \neq 0$, two eigenvalues are

$$\lambda_n^{x,y} = \pm\frac{J_e}{2} + \sqrt{b^2 + J_e^2/4}, \pm\frac{J_e}{2} - \sqrt{b^2 + J_e^2/4}, \quad (130)$$

and the other four eigenvalues satisfy the quartic equation,

$$\begin{aligned}
0 &= x^4 - (3J \mp J_e)x^3 - (4b^2 + 4J_e^2 \pm 3JJ_e)x^2 \\
&\quad +4[3b^2J + JJ_e^2 \pm J_e(b^2 - J_e^2)]x \\
&\quad \pm 4J_e(-3b^2J \pm 2b^2J_e + JJ_e^2). && (131)
\end{aligned}$$

At the first level crossing with $\boldsymbol{B}||\hat{\boldsymbol{z}}$, we have for $J_a \neq 0$,

$$\gamma B_{1,1}^{\mathrm{lc},z} = \frac{1}{2}\Big(J + [9J^2 + 4J_a^2 - 4JJ_a]^{1/2}\Big). \quad (132)$$

At the second level crossing, simple formulas are only obtained for $\boldsymbol{B}||\hat{\boldsymbol{z}}$ with one $J_j \neq 0$. For $\boldsymbol{B}||\hat{\boldsymbol{z}}$ and $J_a \neq 0$, $J_b \neq 0$ and $J_d \neq 0$, respectively, we have

$$\gamma B_{2,1}^{\mathrm{lc},z} = \begin{cases} -2J - J_a, \\ -2J - 3J_b, \\ \frac{1}{3}\Big(20J^2 - 30J_d^2 + 8[4J^4 - 6J^2J_d^2]^{1/2}\Big)^{1/2}. \end{cases} \quad (133)$$

APPENDIX B

Rotation to the induction representation

The rotation from the crystal representation to the induction representation is obtained from

$$\begin{pmatrix} \hat{\boldsymbol{x}} \\ \hat{\boldsymbol{y}} \\ \hat{\boldsymbol{z}} \end{pmatrix} = \begin{pmatrix} \cos\theta\cos\phi & -\sin\phi & \sin\theta\cos\phi \\ \cos\theta\sin\phi & \cos\phi & \sin\theta\sin\phi \\ -\sin\theta & 0 & \cos\theta \end{pmatrix} \begin{pmatrix} \hat{\boldsymbol{x}}' \\ \hat{\boldsymbol{y}}' \\ \hat{\boldsymbol{z}}' \end{pmatrix}, \tag{134}$$

leading to $\boldsymbol{B} = B\hat{\boldsymbol{z}}'$.[25] This operation is equivalent to a rotation by $-\pi/2$ about the z axis, a rotation by θ about the transformed x axis, and then a rotation by $\pi/2-\phi$ about the transformed z axis.[26] In effect, in using the above rotation matrix, we made the arbitrary choice that the rotated z axis lies in the $x'z'$ plane. After the above rotation, it is still possible to rotate the crystal by an arbitrary angle χ about the z' axis, keeping $\boldsymbol{B}||\hat{\boldsymbol{z}}'$. Hence, there are in effect an infinite number of equivalent rotations leading to $\boldsymbol{B} = B\hat{\boldsymbol{z}}'$. The resulting Hamiltonian matrix will then have off-diagonal elements that depend upon χ. However, all such rotations necessarily lead to the identical, χ-independent, set of eigenvalues of the resulting diagonalized Hamiltonian matrix. We have explicitly checked that the above rotation gives the exact cubic expression, Eq. (43), for the $s_1 = 1/2$ eigenvalues, and also leads to the correct eigenstate energies second order in each of the J_j for $s_1 = 1$. We also showed explicitly that χ does not enter the eigenstate energies second order in J_b for arbitrary s, s_1, m.

Global Hamiltonian

The global axial and azimuthal anisotropy interactions in the rotated frame are

$$\begin{aligned} \mathcal{H}'_b &= -J_b\Big(S^2_{z'}\cos^2\theta + S^2_{x'}\sin^2\theta \\ &\quad - \sin(2\theta)\{S_{x'}, S_{z'}\}/2\Big), \end{aligned} \tag{135}$$

$$\begin{aligned} \mathcal{H}'_d &= -J_d\Big[\cos(2\phi)\Big(S^2_{x'}\cos^2\theta + S^2_{z'}\sin^2\theta - S^2_{y'} \\ &\quad + \sin(2\theta)\{S_{x'}, S_{z'}\}/2\Big) \\ &\quad - \sin(2\phi)\Big(\cos\theta\{S_{x'}, S_{y'}\} + \sin\theta\{S_{y'}, S_{z'}\}\Big)\Big], \end{aligned} \tag{136}$$

where $\{A, B\} = AB + BA$ is the anticommutator.

Global Hamiltonian matrix elements

The operations of the rotated global anisotropy interactions upon these states may be written as

$$\begin{aligned} \mathcal{H}'_b|\varphi^m_s\rangle &= -\frac{J_b}{4}\Big[\Big(4m^2 + 2[s(s+1) - 3m^2]\sin^2\theta\Big)|\varphi^m_s\rangle \\ &\quad - \sin(2\theta)\sum_{\sigma=\pm1}(2m+\sigma)A^{\sigma m}_s|\varphi^{m+\sigma}_s\rangle \\ &\quad + \sin^2\theta\sum_{\sigma=\pm1}F^{\sigma m}_s|\varphi^{m+2\sigma}_s\rangle\Big], \end{aligned} \tag{137}$$

and

$$\begin{aligned} \mathcal{H}'_d|\varphi^m_s\rangle &= -\frac{J_d}{4}\Big(2\sin^2\theta\cos(2\phi)[3m^2 - s(s+1)]|\varphi^m_s\rangle \\ &\quad + 2\sin\theta\sum_{\sigma=\pm1}(2m+\sigma)A^{\sigma m}_s \\ &\quad \times[\cos\theta\cos(2\phi) + i\sigma\sin(2\phi)]|\varphi^{m+\sigma}_s\rangle \\ &\quad + \sum_{\sigma=\pm1}F^{\sigma m}_s\big[(1+\cos^2\theta)\cos(2\phi) \\ &\quad + 2i\sigma\cos\theta\sin(2\phi)\big]|\varphi^{m+2\sigma}_s\rangle\Big), \end{aligned} \tag{138}$$

where F^x_s is defined by Eq. (17). We note that in this representation, both $\mathcal{H}_b$ and $\mathcal{H}_d$ preserve the global spin quantum number s, but allow $\Delta m = \pm1, \pm2$ transitions. As a check on the algebra, we verified that for $s_1 = 1/2$, Eq. (43) with $J_a = J_c = 0$ is obtained from Eqs. (137) and (138).

Local Hamiltonian

With regard to the local spin anisotropy terms in the rotated coordinate system, we write

$$\mathcal{H}'_a = -J_a\Big(\mathcal{O}_1\cos^2\theta + \mathcal{O}_2\sin^2\theta - \frac{\sin(2\theta)}{2}\mathcal{O}_3\Big) \tag{139}$$

and

$$\begin{aligned} \mathcal{H}'_e &= -J_e\Big[\cos(2\phi)\Big(\mathcal{O}_1\sin^2\theta + \mathcal{O}_2\cos^2\theta \\ &\quad + \frac{1}{2}\sin(2\theta)\mathcal{O}_3 - \mathcal{O}_4\Big) \\ &\quad - \sin(2\phi)\Big(\mathcal{O}_5\cos\theta + \mathcal{O}_6\sin\theta\Big)\Big], \end{aligned} \tag{140}$$

where

$$\mathcal{O}_1 = \sum_{i=1}^{2}S^2_{iz'}, \tag{141}$$

$$\mathcal{O}_2 = \sum_{i=1}^{2}S^2_{ix'}, \tag{142}$$

$$\mathcal{O}_3 = \sum_{i=1}^{2}(S_{iz'}S_{ix'} + S_{ix'}S_{iz'}), \tag{143}$$

$$\mathcal{O}_4 = \sum_{i=1}^{2} S_{iy'}^2, \tag{144}$$

$$\mathcal{O}_5 = \sum_{i=1}^{2} (S_{ix'}S_{iy'} + S_{iy'}S_{ix'}), \tag{145}$$

and

$$\mathcal{O}_6 = \sum_{i=1}^{2} (S_{iy'}S_{iz'} + S_{iz'}S_{iy'}). \tag{146}$$

Local Hamiltonian matrix element components

The operations of these interactions are given by

$$\mathcal{O}_1|\varphi_s^m\rangle = \frac{1}{2}\Big(G_{s,s_1}^m|\varphi_s^m\rangle + \sum_{\sigma'=\pm1} H_{s,s_1}^{m,\sigma'}|\varphi_{s+2\sigma'}^m\rangle\Big), \tag{147}$$

$$\mathcal{O}_2|\varphi_s^m\rangle = \frac{1}{8}\Big(M_{s,s_1}^m|\varphi_s^m\rangle - \sum_{\sigma'=\pm1} N_{s,s_1}^{m,\sigma'}|\varphi_{s+2\sigma'}^m\rangle + \sum_{\sigma=\pm1} L_{s,s_1}^{\sigma m}|\varphi_s^{m+2\sigma}\rangle + \sum_{\sigma,\sigma'=\pm1} K_{s,s_1}^{\sigma m,\sigma'}|\varphi_{s+2\sigma'}^{m+2\sigma}\rangle\Big), \tag{148}$$

$$\mathcal{O}_3|\varphi_s^m\rangle = \frac{1}{4}\sum_{\sigma=\pm1}\Big(P_{s,s_1}^{m,\sigma}|\varphi_s^{m+\sigma}\rangle - \sum_{\sigma'=\pm1}\sigma\sigma' R_{s,s_1}^{\sigma m,\sigma'}|\varphi_{s+2\sigma'}^{m+\sigma}\rangle\Big), \tag{149}$$

$$\mathcal{O}_4|\varphi_s^m\rangle = \frac{1}{8}\Big(M_{s,s_1}^m|\varphi_s^m\rangle - \sum_{\sigma'=\pm1} N_{s,s_1}^{m,\sigma'}|\varphi_{s+2\sigma'}^m\rangle - \sum_{\sigma=\pm1} L_{s,s_1}^{\sigma m}|\varphi_s^{m+2\sigma}\rangle - \sum_{\sigma,\sigma'=\pm1} K_{s,s_1}^{\sigma m,\sigma'}|\varphi_{s+2\sigma'}^{m+2\sigma}\rangle\Big), \tag{150}$$

$$\mathcal{O}_5|\varphi_s^m\rangle = \frac{1}{4i}\sum_{\sigma=\pm1}\sigma\Big(L_{s,s_1}^{\sigma m}|\varphi_s^{m+2\sigma}\rangle + \sum_{\sigma'=\pm1} K_{s,s_1}^{\sigma m,\sigma'}|\varphi_{s+2\sigma'}^{m+2\sigma}\rangle\Big), \tag{151}$$

$$\mathcal{O}_6|\varphi_s^m\rangle = \frac{1}{4i}\sum_{\sigma=\pm1}\Big(\sigma P_{s,s_1}^{m,\sigma}|\varphi_s^{m+\sigma}\rangle - \sum_{\sigma'=\pm1}\sigma' R_{s,s_1}^{\sigma m,\sigma'}|\varphi_{s+2\sigma'}^{m+\sigma}\rangle\Big), \tag{152}$$

where

$$M_{s,s_1}^m = -4m^2\alpha_{s,s_1} + 4[s(s+1)-1](1-\alpha_{s,s_1}), \tag{153}$$

$$N_{s,s_1}^{m,\sigma'} = \sum_{\sigma=\pm1} C_{s+(\sigma'+1)/2,s_1}^{-\sigma\sigma' m-(\sigma'+1)/2} C_{s+(3\sigma'+1)/2,s_1}^{\sigma\sigma' m+(\sigma'-1)/2}, \tag{154}$$

$$P_{s,s_1}^{m,\sigma} = 2A_s^{\sigma m}(2m+\sigma)\alpha_{s,s_1}, \tag{155}$$

and

$$R_{s,s_1}^{x,\sigma'} = C_{s+(\sigma'+1)/2,s_1}^{-x\sigma'-(\sigma'+1)/2} D_{s+(3\sigma'+1)/2,s_1}^{m+\sigma} + C_{s+(3\sigma'+1)/2,s_1}^{-x\sigma'-(\sigma'+1)/2} D_{s+(\sigma'+1)/2,s_1}^{m}, \tag{156}$$

where η_{s,s_1}, G_{s,s_1}^m, $H_{s,s_1}^{m,\sigma'}$, $K_{s,s_1}^{x,\sigma'}$, and L_{s,s_1}^x are given by Eqs. (22) and (25)-(28), respectively. We note that for $\sigma' = \pm1$, $N_{s,s_1}^{m,\sigma'} = 2H_{s,s_1}^{m,\sigma'}$.

APPENDIX C

Second order induction representation Hamiltonian

In this appendix, we evaluate the corrections to the eigenstate energies second order in the four anisotropy interaction energies J_j for $j = a, b, d, e$. The operations of the rotated Hamilatonian $\mathcal{H}'$ upon the eigenstates $|\varphi_s^m\rangle$ may be written as

$$\mathcal{H}'|\varphi_s^m\rangle = (E_s^{m,(0)} + E_{s,s_1}^{m,(1)})|\varphi_s^m\rangle + \sum_{\sigma'=\pm1}\mathcal{W}_{s,s_1}^{m,\sigma'}|\varphi_{s+2\sigma'}^m\rangle + \sum_{\sigma=\pm1}\Big(\mathcal{U}_{s,s_1}^{m,\sigma}|\varphi_s^{m+\sigma}\rangle + \mathcal{V}_{s,s_1}^{m,\sigma}|\varphi_s^{m+2\sigma}\rangle\Big) + \sum_{\sigma,\sigma'=\pm1}\Big(\mathcal{X}_{s,s_1}^{m,\sigma,\sigma'}|\varphi_{s+2\sigma'}^{m+\sigma}\rangle + \mathcal{Y}_{s,s_1}^{m,\sigma,\sigma'}|\varphi_{s+2\sigma'}^{m+2\sigma}\rangle\Big), \tag{157}$$

where

$$\mathcal{U}_{s,s_1}^{m,\sigma}(\theta,\phi) = \frac{1}{4}(2m+\sigma)A_s^{\sigma m}\Big[\sin(2\theta)\Big(\tilde{J}_{b,a}^{s,s_1} - \tilde{J}_{d,e}^{s,s_1}\cos(2\phi)\Big) - 2i\sigma\tilde{J}_{d,e}^{s,s_1}\sin\theta\sin(2\phi)\Big], \tag{158}$$

$$\mathcal{V}_{s,s_1}^{m,\sigma}(\theta,\phi) = -\frac{1}{4}F_s^{\sigma m}\Big[\tilde{J}_{b,s}^{s,s_1}\sin^2\theta + \tilde{J}_{d,e}^{s,s_1}(1+\cos^2\theta)\cos(2\phi) + 2i\sigma\tilde{J}_{d,e}^{s,s_1}\cos\theta\sin(2\phi)\Big], \tag{159}$$

$$\mathcal{W}_{s,s_1}^{m,\sigma'}(\theta,\phi) = -\frac{1}{2}H_{s,s_1}^{m,\sigma'}[J_a\cos^2\theta + J_e\sin^2\theta\cos(2\phi)] + \frac{1}{8}N_{s,s_1}^{m,\sigma'}\sin^2\theta[J_a - J_e\cos(2\phi)], \tag{160}$$

$$\mathcal{X}_{s,s_1}^{m,\sigma,\sigma'}(\theta,\phi) = -\frac{\sigma\sigma'}{8}R_{s,s_1}^{\sigma m,\sigma'}\Big(\sin(2\theta)[J_a - J_e\cos(2\phi)] - 2i\sigma J_e\sin\theta\sin(2\phi)\Big), \tag{161}$$

and

$$\mathcal{Y}_{s,s_1}^{\sigma m,\sigma'}(\theta,\phi) = -\frac{1}{8}K_{s,s_1}^{\sigma m,\sigma'}\Big[J_a\sin^2\theta + J_e\Big((1+\cos^2\theta)\cos(2\phi)$$

$$+2i\sigma\cos\theta\sin(2\phi)\Big)\Big], \qquad (162)$$

where $E^{m,(0)}_{s,s_1}$ and $E^{m,(1)}_{s,s_1}$ are given by Eqs. (65) and (66), respectively, $H^{m,\sigma'}_{s,s_1}$ and $K^{x,\sigma'}_{s,s_1}$ are given by Eqs. (26) and (27), respectively, $N^{m,\sigma'}_{s,s_1}$ and $R^{x,\sigma'}_{s,s_1}$ are given by Eqs. (154) and (156), respectively, and $\tilde{J}^{s,s_1}_{b,a}$ and $\tilde{J}^{s,s_1}_{d,e}$ are given by Eqs. (67) and (68), respectively.

Second order eigenstate energies

From Eq. (157), the second order eigenstate energies may be written as

$$\begin{aligned}
E^{m,(2)}_{s,s_1} &= \frac{1}{\gamma B}\sum_{\sigma=\pm1}\sigma\Big(\Big|\mathcal{U}^{m,\sigma}_{s,s_1}\Big|^2+\frac{1}{2}\Big|\mathcal{V}^{m,\sigma}_{s,s_1}\Big|^2\Big)\\
&+\sum_{\sigma'=\pm1}\frac{|\mathcal{W}^{m,\sigma'}_{s,s_1}|^2}{J[2+(2s+1)\sigma']}\\
&+\sum_{\sigma,\sigma'\pm1}\Big(\frac{|\mathcal{X}^{m,\sigma,\sigma'}_{s,s_1}|^2}{J[2+(2s+1)\sigma']+\sigma\gamma B}\\
&+\frac{|\mathcal{Y}^{m,\sigma,\sigma'}_{s,s_1}|^2}{J[2+(2s+1)\sigma']+2\sigma\gamma B}\Big). \qquad (163)
\end{aligned}$$

For simplicity, we rewrite this as

$$\begin{aligned}
E^{m,(2)}_{s,s_1} &= E^{m,(2)\mathcal{U}}_{s,s_1}+E^{m,(2)\mathcal{V}}_{s,s_1}+E^{m,(2)\mathcal{W}}_{s,s_1}\\
&+E^{m,(2)\mathcal{X}}_{s,s_1}+E^{m,(2)\mathcal{Y}}_{s,s_1}, \qquad (164)\\
E^{m,(2)\mathcal{U}}_{s,s_1} &= \frac{m\sin^2\theta}{2\gamma B}[4s(s+1)-8m^2-1]\\
&\times\Big(\cos^2\theta[\tilde{J}^{s,s_1}_{b,a}-\cos(2\phi)\tilde{J}^{s,s_1}_{d,e}]^2\\
&+\sin^2(2\phi)(\tilde{J}^{s,s_1}_{d,e})^2\Big), \qquad (165)\\
E^{m,(2)\mathcal{V}}_{s,s_1} &= -\frac{m}{8\gamma B}[2s(s+1)-2m^2-1]\\
&\times\Big([\sin^2\theta\tilde{J}^{s,s_1}_{b,a}+(1+\cos^2\theta)\cos(2\phi)\tilde{J}^{s,s_1}_{d,e}]^2\\
&+4\cos^2\theta\sin^2(2\phi)(\tilde{J}^{s,s_1}_{d,e})^2\Big), \qquad (166)\\
E^{m,(2)\mathcal{W}}_{s,s_1} &= \frac{d^m_{s,s_1}}{16J}\Big(J_a-3[J_a\cos^2\theta+J_e\sin^2\theta\cos(2\phi)]\Big)^2, \qquad (167)\\
E^{m,(2)\mathcal{X}}_{s,s_1} &= \frac{f^m_{s,s_1}(\gamma B/J)\sin^2\theta}{2J}\\
&\times\Big([J_a-J_e\cos(2\phi)]^2\cos^2\theta\\
&+\sin^2(2\phi)J_e^2\Big), \qquad (168)\\
E^{m,(2)\mathcal{Y}}_{s,s_1} &= \frac{g^m_{s,s_1}(\gamma B/J)}{64J}\Big[\Big(J_a\sin^2\theta\\
&+J_e(1+\cos^2\theta)\cos(2\phi)\Big)^2\\
&+4\cos^2\theta\sin^2(2\phi)J_e^2\Big], \qquad (169)
\end{aligned}$$

where

$$\begin{aligned}
d^m_{s,s_1} &= -\frac{(s^2-m^2)[(s-1)^2-m^2]\eta^2_{s,s_1}\eta^2_{s-1,s_1}}{(2s-1)}\\
&+\eta^2_{s+2,s_1}\eta^2_{s+1,s_1}\\
&\times\frac{[(s+1)^2-m^2][(s+2)^2-m^2]}{(2s+3)},\\
f^m_{s,s_1}(x) &= -\frac{\eta^2_{s,s_1}\eta^2_{s-1,s_1}(s^2-m^2)}{(2s-1)^2-x^2}\\
&\times\Big((2s-1)[(s-1)(s-2)+m^2]\\
&-m(2s-3)x\Big)\\
&+\frac{\eta^2_{s+2,s_1}\eta^2_{s+1,s_1}[(s+1)^2-m^2]}{(2s+3)^2-x^2}\\
&\times\Big((2s+3)[(s+2)(s+3)+m^2]\\
&-m(2s+5)x\Big), \qquad (170)\\
g^m_{s,s_1}(x) &= \frac{2\eta^2_{s,s_1}\eta^2_{s-1,s_1}}{(2s-1)^2-4x^2}\Big((2s-1)[m^4\\
&+m^2(6s^2-18s+11)\\
&+s(s-1)(s-2)(s-3)]\\
&-4mx(2s-3)(s^2-3s+1+m^2)\Big) \qquad (171)\\
&-\frac{2\eta^2_{s+2,s_1}\eta^2_{s+1,s_1}}{(2s+3)^2-4x^2}\Big((2s+3)[m^4\\
&+m^2(6s^2+29s+34)\\
&+(s+1)(s+2)(s+3)(s+4)]\\
&-4mx(2s+5)(s^2+5s+5+m^2)\Big). \qquad (172)
\end{aligned}$$

There is a remarkable amount of symmetry in the angular dependence of the eigenstate energies. We note that $E^{m,(2)\mathcal{X}}_{s,s_1}(\theta,\phi)$ and $E^{m,(2)\mathcal{U}}_{s,s_1}(\theta,\phi)$ have the same forms, differing in the replacements of the interactions $\tilde{J}^{s,s_1}_{b,a}$ and $\tilde{J}^{s,s_1}_{d,e}$ with J_a and J_e, respectively, and with different overall constant functions. The same comparison can also be made with $E^{m,(2)\mathcal{Y}}_{s,s_1}(\theta,\phi)$ and $E^{m,(2)\mathcal{V}}_{s,s_1}(\theta,\phi)$. In addition, we note that there is a remarkable similarity in the θ,ϕ dependence of $E^{m,(2)\mathcal{W}}_{s,s_1}$ with that of the local spin anisotropy part of $B^{\mathrm{lc}(1)}_{s,s_1}(\theta,\phi)$ in Eq. (73).

APPENDIX D

The contributions to the sth level crossing second order in the anisotropy interactions are calculated as indicated in Eq. (74), and are found to be

$$\Big(E^{s,(2)}_{s,s_1}-E^{s-1,(2)}_{s-1,s_1}\Big)\Big|_{B=-Js/\gamma} = \sum_{n=1}^{7}a_n(s,s_1)f_n(\theta,\phi).$$

(173)

Second order level crossing angular functions

$$f_1(\theta,\phi) = \frac{\sin^2\theta}{J}\Big([J_b-\cos(2\phi)J_d]^2\cos^2\theta + J_d^2\sin^2(2\phi)\Big), \quad (174)$$

$$f_2(\theta,\phi) = \frac{\sin^2\theta}{J}\Big([J_b-J_d\cos(2\phi)][J_a-J_e\cos(2\phi)] \times\cos^2\theta + J_dJ_e\sin^2(2\phi)]\Big), \quad (175)$$

$$f_3(\theta,\phi) = \frac{\sin^2\theta}{J}\Big([J_a-\cos(2\phi)J_e]^2\cos^2\theta + J_e^2\sin^2(2\phi)\Big), \quad (176)$$

$$f_4(\theta,\phi) = \frac{1}{J}\Big(J_b\sin^2\theta+J_d(1+\cos^2\theta)\cos(2\phi)\Big)^2 +4\frac{J_d^2}{J}\cos^2\theta\sin^2(2\phi), \quad (177)$$

$$f_5(\theta,\phi) = \frac{1}{J}[J_b\sin^2\theta+J_d(1+\cos^2\theta)\cos(2\phi)] \times[J_a\sin^2\theta+J_e(1+\cos^2\theta)\cos(2\phi)] +4\frac{J_dJ_e}{J}\cos^2\theta\sin^2(2\phi), \quad (178)$$

$$f_6(\theta,\phi) = \frac{1}{J}\Big(J_a\sin^2\theta+J_e(1+\cos^2\theta)\cos(2\phi)\Big)^2 +4\frac{J_e^2}{J}\cos^2\theta\sin^2(2\phi), \quad (179)$$

$$f_7(\theta,\phi) = \frac{1}{J}\Big(J_a-3[J_a\cos^2\theta+J_e\sin^2\theta\cos(2\phi)]\Big)^2. \quad (180)$$

Second order level crossing coefficients

The coefficients are given by

$$a_1(s,s_1) = -\frac{(8s-9)}{2s}, \quad (181)$$

$$a_2(s,s_1) = -\frac{[a_{2,0}(s)+4s_1(s_1+1)a_{2,1}(s)]}{s(2s+1)(2s+3)}, \quad (182)$$

$$a_{2,0}(s) = -3(9+s-23s^2+4s^3+12s^4),$$

$$a_{2,1}(s) = -9+8s+4s^2, \quad (183)$$

$$a_3(s,s_1) = a_3^{\mathcal{U}}(s,s_1)+a_3^{\mathcal{X}}(s,s_1), \quad (184)$$

$$a_3^{\mathcal{U}}(s,s_1) = \frac{[3-3s-3s^2+4s_1(s_1+1)]^2}{2(2s+3)^2} -\frac{(s-1)[3+3s-3s^2+4s_1(s_1+1)]^2}{2s(2s+1)^2}, \quad (185)$$

$$a_3^{\mathcal{X}}(s,s_1) = \frac{[s(s+2)-4s_1(s_1+1)]}{2(s+1)(s+3)(2s+1)^2(2s+3)^2} \times\frac{a_{3,0}^{\mathcal{X}}(s)+4s_1(s_1+1)a_{3,1}^{\mathcal{X}}(s)}{(2s+5)(3s+1)},$$

$$a_{3,0}^{\mathcal{X}}(s) = (s+1)(s+3)(51+114s +209s^2+302s^3+164s^4+24s^5), \quad (186)$$

$$a_{3,1}^{\mathcal{X}}(s) = 129+318s+395s^2 +442s^3+300s^4+72s^5,$$

$$a_4(s,s_1) = \frac{(4s-3)}{8s}, \quad (187)$$

$$a_5(s,s_1) = -\frac{3[a_{5,0}(s)+4s_1(s_1+1)]}{4s(2s+1)(2s+3)}, \quad (188)$$

$$a_{5,0}(s) = 3+3s-5s^2-4s^3, \quad (189)$$

$$a_6(s,s_1) = a_6^{\mathcal{V}}(s,s_1)+a_6^{\mathcal{Y}}(s,s_1), \quad (190)$$

$$a_6^{\mathcal{V}}(s,s_1) = \frac{[3-3s-3s^2+4s_1(s_1+1)]^2}{8(2s-1)(2s+3)^2} -\frac{(s-1)[3+3s-3s^2+4s_1(s_1+1)]^2}{8s(2s-3)(2s+1)^2}, \quad (191)$$

$$a_6^{\mathcal{Y}}(s,s_1) = \frac{-1}{96(2s-3)(2s-1)(2s+1)^2(2s+3)^2} \times\frac{\sum_{n=0}^{2}a_{6,n}^{\mathcal{Y}}(s)[4s_1(s_1+1)]^n}{(2s+5)(4s+1)(4s+3)},$$

$$a_{6,0}^{\mathcal{Y}}(s) = s\Big(-5184+20898s+123003s^2 +81669s^3-304665s^4-521611s^5 -168482s^6+163132s^7+124888s^8 +12008s^9+256s^{10}+128s^{11}\Big), \quad (192)$$

$$a_{6,1}^{\mathcal{Y}}(s) = 5832+6939s+855s^2+17694s^3 +22242s^4-1548s^5-3464s^6 +3728s^7+1920s^8-512s^9-256s^{10}, \quad (193)$$

$$a_{6,2}^{\mathcal{Y}}(s) = 4536+5787s-3111s^2+4782s^3 +16972s^4+5144s^5-864s^6 +256s^7+128s^8, \quad (194)$$

$$a_7(s,s_1) = \frac{[s(s+2)-4s_1(s_1+1)]}{4(2s+1)^3(2s+3)^3(2s+5)} \times\Big(4s_1(s_1+1)(-1+38s+24s^2+60s^3) +(s+1)(3+67s+94s^2+44s^3+8s^4)\Big). \quad (195)$$

By expanding the solutions in the crystal representation to second order in the J_j, we have explicitly checked these expressions for $s_1 = 1/2, s = 1$, and for $s_1 = 1$, $s = 1, 2$. We note that for $s_1 = 1/2$, only a_1 and a_4 are non-vanishing.

* Electronic address: efremov@theory.phy.tu-dresden.de
† Electronic address: klemm@phys.ksu.edu

[1] R. Sessoli, D. Gatteschi, A. Caneschi, and M. A. Novak, Nature (London) **365**, 141 (1993).
[2] J. R. Friedman, M. P. Sarachik, J. Tejada, and R. Ziolo, Phys. Rev. Lett. **76**, 3830 (1996).
[3] M. N. Leuenberger and D. Loss, Nature (London) **410**, 789 (2001).
[4] W. Wernsdorfer, T. Ohm, C. Sangregorio, R. Sessoli, D. Mailly, and C. Paulsen, Phys. Rev. Lett. **82**, 3903 (1999).
[5] W. Wernsdorfer and R. Sessoli, Science **284**, 133 (1999).
[6] D. Zipse, J. M. North, N. S. Dalal, S. Hill, and R. S. Edwards, Phys. Rev. B **68**, 184408 (2003).
[7] M. Affronte, A. Cornia, A. Lascialfari, F. Borsa, D. Gatteschi, J. Hinderer, M. Horvatić, A. G. M. Jansen, and M.-H. Julien, Phys. Rev. Lett. **88**, 167201 (2002).
[8] O. Waldmann, J. Schülein, R. Koch, P. Müller, I. Bernt, R. W. Saalfrank, H. P. Andres, H. U. Güdel, and P. Allenspach, Inorg. Chem. **38**, 5879 (1999).
[9] O. Waldmann, R. Koch, S. Schromm, J. Schülein, P. Müller, I. Bernt, R. W. Saalfrank, F. Hempel, and E. Balthes, Inorg. Chem. **40**, 2986 (2001).
[10] H. Nakano and S. Miyashita, J. Phys. Chem. Solids **63**, 1519 (2002).
[11] D. A. Tennant, S. E. Nagler, A. W. Garrett, T. Barnes, and C. C. Torardi, Phys. Rev. Lett. **78**, 4998 (1997).
[12] H. U. Güdel, Neutron News **7**, 24 (1996)
[13] A. W. Garrett, S. E. Nagler, D. A. Tennant, B. C. Sales, and T. Barnes, Phys. Rev. Lett. **79**, 745 (1997).
[14] D. V. Efremov and R. A. Klemm, Phys. Rev. B **66**, 174427 (2002).
[15] F. Le Gall, F. Fabrizi de Biani, A. Caneschi, P. Cinelli, A. Cornia, A. C. Fabretti, and D. Gatteschi, Inorg. Chim. Acta **262**, 123 (1997).
[16] Y. Shapira, M. T. Liu, S. Foner, R. J. Howard, and W. H. Armstrong, Phys. Rev. B **63**, 094422 (2001).
[17] Y. Shapira, M. T. Liu, S. Foner, C. E. Dubé, and P. J. Bonitatebus, Jr., Phys. Rev. B **59**, 1046 (1999).
[18] K. L. Taft, C. D. Delfs, G. C. Papaefthymiou, S. Foner, D. Gatteschi, and S. J. Lippard, J. Am. Chem. Soc. **116**, 823 (1994).
[19] J. D. Walker and R. Poli, Inorg. Chem. **29**, 756 (1990).
[20] J. A. Bertrand, J. L. Breece, and P. G. Eller, Inorg. Chem. **13**, 125 (1974).
[21] R. Tiron, W. Wernsdorfer, D. Foquet-Albiol, N. Aliaga-Alcalde, and G. Christou, Phys. Rev. Lett. **91**, 227203 (2003).
[22] J. M. North, N. S. Dalal, D. Foquet-Albiol, A. Vinslava, and G. Christou, Phys. Rev. B **69**, 174419 (2004).
[23] O. Waldmann, J. Hassmann, P. Müller, D. Volkmer, U. S. Schubert, and J.-M. Lehn, Phys. Rev. B **58**, 3277 (1998).
[24] J. J. Borrás-Almenar, J. M. Clemente-Juan, E. coronado, and B. S. Tsukerblat, Inorg. Chem. **38**, 6081 (1999).
[25] R. A. Klemm and J. R. Clem, Phys. Rev. B **21**, 1868 (1980); R. A. Klemm, SIAM J. Appl. Math. **55**, 986 (1995).
[26] H. Goldstein, *Classical Mechanics*, (Addison-Wesley, Reading, MA 1965), p. 109.